

ALAN CORNEY

ATOMIC  
AND  
LASER  
SPECTROSCOPY

Auszüge

CLarendon Press · oxford  
1977



16. OPTICAL DOUBLE RESONANCE EXPERIMENTS	534	17. OPTICAL PUMPING EXPERIMENTS	592
16.1. Magnetic resonance and excited atoms	534	17.1. Introduction	592
16.2. Theory of the Brossel-Bitter experiment	539	17.2. Principles of optical pumping	593
16.3. Discussion of the optical double-resonance method	548	17.3. Effect of relaxation processes	601
16.4. Radiation trapping and coherence narrowing	551	17.4. Investigation of longitudinal relaxation times	604
16.5. Collision broadening in resonance fluorescence experiments	557	17.5. Spin-exchange collisions	615
16.6. Light modulation in double-resonance experiments	572	17.6. Optical pumping of metastable atoms	616
16.7. Magnetic resonance in the density matrix formalism	576	17.7. Optical pumping and magnetic resonance	619
16.8. Expansion of the density matrix in terms of irreducible tensor operators	584	17.8. Transverse magnetization and Hertzian coherence in optical pumping experiments	629
Problems	586	17.9. Quantum theory of the optical pumping cycle	639
References	589	Problems	654
<u>General references and further reading</u>	590	References	658
		<u>General references and further reading</u>	659
18. THE HYPERFINE STRUCTURE OF ATOMS AND ITS INVESTIGATION BY MAGNETIC RESONANCE METHODS	661		
18.1. Theory of hyperfine structure	662		
18.2. Investigation of hyperfine structure of ground-state atoms by optical pumping	676		
18.3. Hyperfine pumping and the measurement of $v_{HFS}$	682		
18.4. Optically pumped rubidium frequency standards	680		
18.5. The atomic beam magnetic resonance technique	692		
18.6. Hyperfine structure investigations by the atomic beam technique	701		
18.7. Cesium beam atomic clock	705		
18.8. Hyperfine structure of atomic hydrogen	708		
18.9. Investigation of the hyperfine structure of excited states	714		
18.10. Conclusion	730		
Problems	731		
References	738		
<u>General references and further reading</u>	740		



## Optical double resonance experiments

### 16.1. Magnetic resonance and excited atoms

16.1.1. Introduction. In our discussion of the Hanle effect in the previous chapter, we assumed that the g-factors of the excited atomic levels were already well known or could be calculated to sufficient accuracy from the Landé formula

$$g_J = g_L \{J(J+1) + L(L+1) - S(S+1)\}/2J(J+1) + \\ + g_S \{J(J+1) + S(S+1) - L(L+1)\}/2J(J+1).$$

However, in the spectra of mercury and many other elements the existence of intercombination lines shows that L-S coupling does not hold rigorously and that small deviations of the actual g-factors from the L-S values may be observed. These deviations contain useful information about the atomic wavefunctions and a technique which would permit the accurate measurement of the Zeeman splittings of excited levels is clearly very desirable. It would also be interesting to make accurate measurements of the hyperfine structures of the excited levels of odd isotopes since these give information about the magnetic dipole and electric quadrupole moments of the atomic nucleus.

Unfortunately, however, conventional techniques of high-resolution optical spectroscopy are limited by the large Doppler widths of spectral lines, typically of the order of  $0.050 \text{ cm}^{-1} \approx 1500 \text{ MHz}$ . Many of the hyperfine structure intervals that must be measured lie in the range  $(3-30) \times 10^{-3} \text{ cm}^{-1} \approx (90-900) \text{ MHz}$  and low field Zeeman splittings are generally even smaller. Thus the techniques of optical spectroscopy are incapable of achieving the required resolution or precision. This is mainly due to the fact that a small energy separation is being measured indirectly by taking the difference between two very large optical frequencies. From equation (8.42) we recall that the Doppler width is proportional to the observed frequency.

If, therefore, some means could be devised to measure the splittings between the excited levels directly, then the Doppler width associated with the signal would be reduced to a negligible value.

This desirable result is in fact achieved in the magnetic resonance technique, which is well known in atomic beam experiments and in solid state physics. In investigations of ground-state Zeeman splittings by this method, the atoms are subjected to a static magnetic field  $\underline{B} = B\underline{k}$  which splits the magnetic sublevels by an amount  $\hbar\omega_L$  where  $\omega_L = g_J \mu_B B/h$  is the Larmor angular frequency. In addition the atoms experience a time dependent field  $\underline{B}_1$  which rotates in a plane perpendicular to  $\underline{B}$  at the angular frequency  $\omega_0$ . The coils which generate this magnetic field may be regarded as a source of radio frequency photons having an energy  $\hbar\omega_0$ . When the frequency of the r.f. field is such that  $\omega_0 = \omega_L$ , magnetic dipole transitions are induced between the levels with the absorption or stimulated emission of quanta of the radio frequency field. In solid state experiments these transitions are usually detected by means of the sharp increase in the r.f. power absorbed by the sample which occurs at resonance. Since the transition probabilities for stimulated emission and absorption between a given pair of states are equal, it is necessary to establish a population difference between them before the resonance can be detected. In solid state experiments this population inequality is provided by the Boltzmann factor  $\sim \exp(-g_J \mu_B B/kT)$  and can be enhanced by working at low temperatures.

For several years it seemed unlikely that the magnetic resonance method could be applied to excited atoms because of the low population of atoms that can be created in excited levels and the high temperatures required to attain appreciable vapour densities. However, it was pointed out by Brossel and Kastler (1949) that the excitation of atoms using polarized resonance radiation allowed very large population differences to be established between excited sub-

levels, and that the change in the polarization of the fluorescent light which occurs at resonance provides an extremely sensitive method of detecting the induced magnetic dipole transitions. This method of studying excited atoms in which optical resonance fluorescence and radio frequency magnetic resonance are combined is known as the *optical double-resonance* technique. We shall now describe the pioneering experiments in this field carried out by Brossel and Bitter (1952).

**16.1.2. Description of the Brossel-Bitter experiment.** The apparatus used by Brossel and Bitter (1952) in the first successful application of the optical double-resonance method is shown in Fig. 16.1(a). The excited  $6^3P_1$  level of mercury was again chosen for study, although similar work on many other elements has been reported subsequently. Light from a low pressure mercury lamp is passed through a linear polarizer oriented so that the electric vector of the radiation is parallel to the constant magnetic field  $\underline{B}$  applied to the atoms in the resonance cell. This field is produced by Helmholtz coils which are not shown in the diagram. With this polarization the incident  $2537 \text{ \AA}$  radiation can only stimulate electric dipole transitions for which  $\Delta m_J = 0$ , Fig. 16.1(b). If we restrict our attention for the moment to the atoms of the even mercury isotopes, only the  $m_J = 0$  state of the excited level is populated. In the absence of other perturbations these atoms would decay after a mean lifetime  $\tau = 1/\Gamma$ , re-emitting light which is also polarized parallel to  $\underline{B}$  ( $\pi$  polarization).

If, however, the excited atoms are subjected to the influence of a strong radio frequency field  $\underline{B}_1$ , rotating in a plane at right-angles to the steady field  $\underline{B}$ , then conditions are right for magnetic resonance to occur. When the Larmor frequency  $\omega_L$  of the excited atoms in the field  $\underline{B}$  approaches the angular frequency  $\omega_0$  of the applied r.f. magnetic field, absorption and stimulated emission of magnetic dipole radiation transfers the atoms to the  $m_J = \pm 1$

states. Since atoms in the  $m_J = \pm 1$  states decay by emitting light which is left and right circularly polarized ( $\sigma^+$  and  $\sigma^-$  respectively in Fig. 16.1(b)), the magnetic dipole transi-

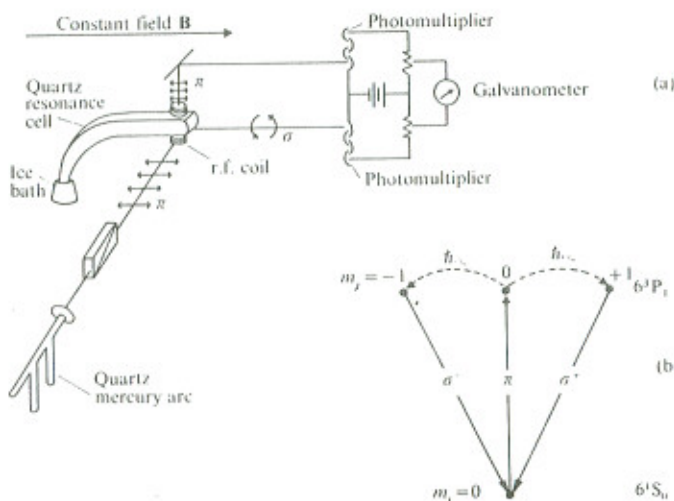


Fig. 16.1. (a) Schematic diagram of the apparatus used by Brossel and Bitter (1952) for optical double-resonance experiments on the  $6^3P_1$  level of mercury. (b) The optical excitation and fluorescent decay processes involved together with the magnetic dipole transitions induced between the Zeeman sub-levels of the  $6^3P_1$  level.

tions will be accompanied by an increase in  $\sigma$ -polarized and a decrease in  $\pi$ -polarized resonance fluorescence. These changes were detected by two photomultipliers which received light emitted in the direction of, and perpendicular to, the field  $\underline{B}$ . The photomultiplier anode currents were sent in opposition through a bridge network which enabled the noise produced by lamp fluctuations to be eliminated and at the same time doubled the observed signal. The difference current was measured on a galvanometer and when

these readings were plotted as a function of the field strength  $B$ , a beautiful set of resonance curves was obtained, as shown in Fig. 16.2. When the strength of the r.f.

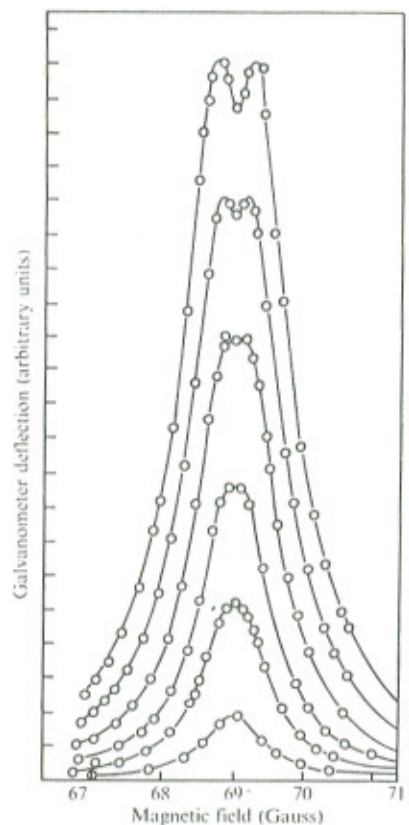


Fig. 16.2. Optical double-resonance signals observed on the  $6^1S_0 - 6^3P_1$  transition of mercury at  $2537 \text{ \AA}$  as a function of the d.c. magnetic field. The curves illustrate the effect of increasing the magnitude of the r.f. field,  $B_1$ . (After Brossel and Bitter (1952).)

magnetic field was increased the amplitude of the signal grew, corresponding to an increase in the stimulated transition probability. The resonance curves also broadened and eventually became double peaked as the stimulated transitions reduced the population differences between excited states.

By measuring the frequency of the r.f. field and calibrating the static field by means of proton resonance, Brossel and Bitter deduced a value for the Landé  $g_J$ -factor of the  $6^3P_1$  level of the even mercury isotopes of

$$g_J = 1.4838 \pm 0.0004.$$

This differs quite significantly from the L-S coupling value (Problem 16.1).

However, the importance of this experiment lies not so much in the result quoted above as in the demonstration of the feasibility of the optical double-resonance method. This pioneering work stimulated renewed interest in resonance fluorescence experiments and opened up a new branch of atomic physics. We shall now derive a detailed expression for the shape of the resonance signal and consider what further information can be obtained by careful studies of the linewidth.

#### 16.2. Theory of the Brossel-Bitter experiment

16.2.1. Classical theory of precession of magnetic dipoles in external magnetic fields. The theory of magnetic resonance can be treated quantum mechanically by introducing into Schrödinger's equation a time-dependent perturbation operator,  $-\mu \cdot \underline{B}(t)$ , representing the combined effect of the magnetic fields applied to the atom. The time-dependent transition probabilities between different magnetic sublevels may then be calculated. It is instructive, however, to approach the calculation first from the classical point of view and to attempt to describe the motion of a classical magnetic dipole moment  $\mu$  in the combination of static and time-dependent fields. The ideas developed in this discussion of magnetic resonance experiments are useful in many

situations and moreover they lead to expressions for the shape of optical double-resonance signals which are in agreement with observations for the case of an excited level with  $J_e=1$  decaying to a ground state with  $J_g=0$ .

(a) Precession in a static magnetic field. We first examine the behaviour of a magnetic dipole moment  $\underline{\mu}$  in a static magnetic field  $\underline{B}=B\hat{k}$  pointing along the  $z$ -axis. The magnetic dipole moment is assumed to be associated with an angular momentum vector  $\underline{hJ}$  by the relation  $\underline{\mu}=-\gamma\underline{hJ}$  where  $\gamma=g_J\mu_B/\hbar$  is called the magneto-gyric ratio. The magnetic dipole experiences a torque which acts to change the direction of the angular momentum vector, giving the equation of motion

$$\hbar \frac{d\underline{J}}{dt} = \underline{\mu} \wedge \underline{B}. \quad (16.1)$$

Substituting for  $\underline{J}$  in this equation we have

$$\frac{d\underline{\mu}}{dt} = -\gamma \underline{\mu} \wedge \underline{B}. \quad (16.2)$$

It is not difficult to show (Problem 16.2) that the steady state solution of equation (16.2) may be written in the form

$$\begin{aligned}\mu_x &= \mu \sin\theta \cos\omega_L t \\ \mu_y &= \mu \sin\theta \sin\omega_L t \\ \mu_z &= \mu \cos\theta.\end{aligned} \quad (16.3)$$

This solution corresponds to a precession of the magnetic dipole about the direction of the magnetic field at the Larmor angular frequency  $\omega_L = \gamma B$  with  $\underline{\mu}$  inclined at some constant but arbitrary angle  $\theta$ , as shown in Fig. 16.3.

(b) Equation of motion in rotating coordinate systems. When we consider a magnetic dipole moment subjected in addition to time-dependent fields, it is first of all appropriate to discuss the motion in a coordinate system which rotates at the angular velocity  $\underline{\omega}_0$  with respect to the laboratory frame. The rate of change  $\partial\underline{A}/\partial t$  of a vector in the rotating frame is related to the rate of change  $d\underline{A}/dt$  in the laboratory frame by

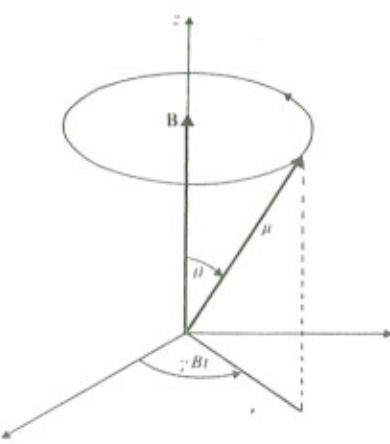


Fig. 16.3. Precession of a magnetic dipole moment  $\underline{\mu}$  about a steady magnetic field  $\underline{B}$ .

$$\frac{\partial \underline{A}}{\partial t} = \frac{d\underline{A}}{dt} - \underline{\omega}_0 \wedge \underline{A}. \quad (16.4)$$

Applying equation (16.4) to the rate of change of  $\underline{\mu}$  given by equation (16.2), we have

$$\frac{\partial \underline{\mu}}{\partial t} = -\gamma \underline{\mu} \wedge \underline{B} - \underline{\omega}_0 \wedge \underline{\mu} = -\gamma \underline{\mu} \wedge (\underline{B} - \underline{\omega}_0/\gamma). \quad (16.5)$$

Thus the equation of motion in the rotating frame is identical to that in the laboratory frame when  $\underline{B}$  is replaced by the effective field

$$\underline{B}_e = \underline{B} - \underline{\omega}_0/\gamma. \quad (16.6)$$

In particular if  $\underline{\omega}_0 = \gamma \underline{B}$  then  $\partial \underline{\mu} / \partial t = 0$  and the magnetic moment is at rest in the rotating frame, thus confirming the solution of the equation of motion given by equation (16.3).

(c) Application to time-dependent fields. We now consider

a magnetic moment  $\underline{\mu}$  subjected simultaneously to a static field  $\underline{B} = \underline{k} \hat{B}$  and a radio frequency field

$$\underline{B}_1 = \hat{x} B_1 \cos \omega_0 t + \hat{y} B_1 \sin \omega_0 t \quad (16.7)$$

which rotates in a plane perpendicular to the z-axis in the counterclockwise sense at the angular frequency  $\omega_0$ . In a coordinate system  $0x'y'z$  which rotates about the z-axis at the same rate (Fig. 16.4) the effective field is

$$\underline{B}_e = \hat{x}' B_1 + \hat{z} (B - \omega_0 / \gamma) \quad (16.8)$$

and is clearly time independent. The magnitude of the effective field is

$$B_e = [B_1^2 + (B - \omega_0 / \gamma)^2]^{1/2} \quad (16.9)$$

and it is inclined at the angle  $\beta$  to the z-axis, where

$$\tan \beta = \frac{B_1}{B - \omega_0 / \gamma} \quad (16.10)$$

From the discussion of section 16.2.1(a), it follows that in the rotating frame the magnetic dipole precesses at the angular frequency  $\omega_e = \gamma B_e$  about the fixed direction of the effective field  $\underline{B}_e$  inclined at a constant arbitrary angle. This precession is indicated in Fig. 16.4. In the rotating frame the vector  $\underline{\mu}$  traces out the surface of a cone whose axis is defined by the direction of the effective field, and the tip of the vector moves on a circle in a plane perpendicular to  $\underline{B}_e$ . In this plane a magnetic dipole  $\underline{\mu}$ , originally created parallel to the z-axis at some time  $t_0$ , will have precessed through the angle  $\psi$  by time  $t$  where

$$\psi = \gamma B_e (t - t_0). \quad (16.11)$$

At this later time  $t$ , the angle  $\alpha$  that the dipole moment makes with the z-axis is obtained by applying the cosine law to the two triangles indicated in Fig. 16.4, giving

$$\cos \alpha = \cos^2 \beta + \sin^2 \beta \cos [\gamma B_e (t - t_0)]. \quad (16.12)$$

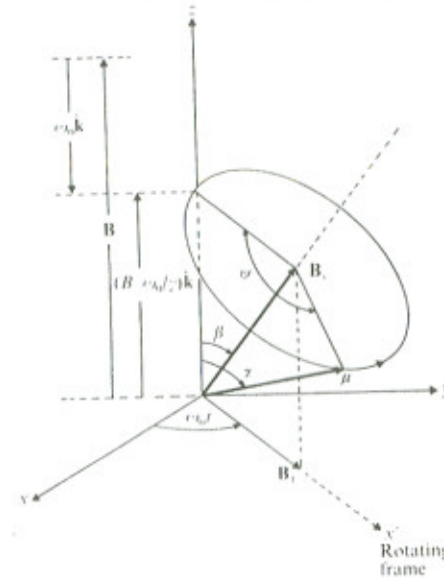


Fig. 16.4. The components of the effective magnetic induction  $\underline{B}_e$  in a coordinate system rotating with the angular velocity  $\omega_0 \hat{k}$ . The field in the laboratory frame is given by  $\hat{x} B_1 \cos \omega_0 t + \hat{y} B_1 \sin \omega_0 t + \hat{z} B$ .

In a combination of static and rotating fields the z-component of the magnetic dipole moment,

$$\mu_z = \mu \cos \alpha, \quad (16.13)$$

is therefore a periodic function of time. On resonance, when  $\omega_L = \omega_0$ , we have  $\beta = \pi/2$  and  $\mu_z$  oscillates sinusoidally between  $\pm \mu$  at a rate determined by the field strength  $B_1$ .

#### 16.2.2. Interpretation in terms of transition probabilities.

This result, derived on the basis of classical mechanics, can now be interpreted quantum mechanically by assuming that the magnetic moment  $\underline{\mu}$  is associated with the spin of an electron. In the laboratory frame the electron wavefunction may be written as a linear superposition of spin up,  $\chi(+1/2)$ , and spin down,  $\chi(-1/2)$ , eigenfunctions:

$$\psi(t) = a_+(t)\chi(+1/2) + a_-(t)\chi(-1/2). \quad (16.14)$$

The expectation value of the magnetic moment of the system is

$$\langle \mu_z \rangle = \langle \psi | -2\mu_B S_z | \psi \rangle = -\mu_B (|a_+|^2 - |a_-|^2). \quad (16.15)$$

Equating equations (16.13) and (16.15), we have

$$|a_+|^2 + |a_-|^2 = \cos \alpha. \quad (16.16)$$

Finally combining this equation with the normalization condition  $|a_+|^2 + |a_-|^2 = 1$  we have

$$\begin{aligned} |a_+|^2 &= (1 - \cos \alpha)/2 = \sin^2(\alpha/2) \\ |a_-|^2 &= (1 + \cos \alpha)/2 = \cos^2(\alpha/2). \end{aligned} \quad (16.17)$$

These equations describe the motion of an electron which at time  $t_0$  was prepared in the spin down state corresponding to a classical dipole moment pointing along the z-axis. Thus the probability of a transition occurring to the spin up state is given by

$$\begin{aligned} P(t, t_0) &= |a_+|^2 = \frac{\sin^2 \gamma B_e (t-t_0)/2}{\omega_1^2} \\ &= \frac{\omega_1^2}{\omega_1^2 + (\omega_L - \omega_0)^2} \sin^2 \{\omega_e (t-t_0)/2\} \end{aligned} \quad (16.18)$$

where  $\omega_1 = \gamma B_1$  and  $\omega_e = \gamma B_e$ . On resonance the electron oscillates periodically between the spin-down and the spin-up states, as shown in Fig. 16.5. The rate at which the transition occurs is determined by the strength of the rotating field  $B_1$ . The classical precession of the magnetic dipole moment in the combined magnetic fields can therefore be interpreted quantum mechanically in terms of magnetic dipole transitions stimulated by the applied radio-frequency field  $B_1$  (Problem 16.3).

16.2.3. Magnetic dipole transitions between isolated excited states. We now consider magnetic dipole transitions between two isolated excited atomic states which have the same

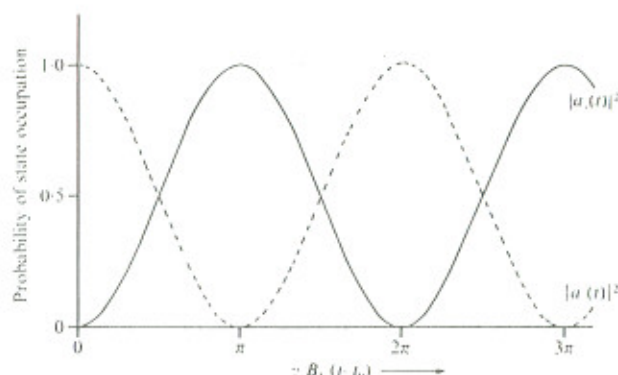


Fig. 16.5. A plot of the time-dependent probabilities,  $|a_+(t)|^2$  and  $|a_-(t)|^2$ , of finding an electron in the  $m_s = +\frac{1}{2}$  and  $m_s = -\frac{1}{2}$  states respectively. The electron was prepared in the  $m_s = -\frac{1}{2}$  state at time  $t=t_0$  and the magnetic resonance condition  $\omega_0 = \gamma B = \omega_L$ , is assumed to be satisfied exactly.

radiative decay rate  $\Gamma$ . This calculation would apply to the Brossel-Bitter experiment, for example, if the fluorescent light was transmitted through a circular polarizer, thus allowing the increase in the  $\sigma^+$  polarized radiation alone to be measured. We are then concerned only with transitions from the  $m_J=0$  to the  $m_J=\pm 1$  states. The intensity of light emitted at time  $t$  by atoms which were prepared in the state  $m_J=0$  at time  $t_0$  is given by

$$I(t, t_0) = I_0 P(t, t_0) \exp\{-\Gamma(t-t_0)\} \quad (16.19)$$

where  $P(t, t_0)$  is the magnetic resonance transition probability and the exponential factor takes account of the radiative decay of the excited atoms. Using equation (16.18) the resonance fluorescence signal obtained from a sample of atoms which are excited at a uniform rate  $R$  from  $t_0 = -\infty$  is

$$\begin{aligned}
 I &= R \int_{-\infty}^t I(t, t_0) dt_0 \\
 &= I_0 R \left\{ \frac{\omega_1^2}{\omega_1^2 + (\omega_L - \omega_0)^2} \right\} \int_{-\infty}^t \sin^2 \{\omega_e(t-t_0)/2\} \exp\{-\Gamma(t-t_0)\} dt_0 \\
 &= \frac{RI_0}{\Gamma} \frac{\omega_1^2}{\omega_1^2 + (\omega_L - \omega_0)^2}. \tag{16.20}
 \end{aligned}$$

Not unexpectedly this is a Lorentzian-shaped signal centred at the magnetic field  $B_0 = \omega_0/\gamma$ . The full width at half the maximum intensity,

$$\Delta\omega_{1/2} = 2(\Gamma^2 + \gamma^2 B_1^2)^{1/2}, \tag{16.21}$$

is determined, at low r.f. powers, by the radiative widths of the two energy levels involved. The magnetic dipole transitions stimulated by the external r.f. field artificially shorten the lifetime of the states and lead to the power broadening of the resonance signals which is evident in Fig. 16.2. This power broadening is expressed quantitatively in equation (16.21).

16.2.4. Derivation of the Brossel-Bitter formula. In a static magnetic field the  ${}^6S_1$  level of mercury splits into three magnetic sub-states which are essentially equally spaced for fields less than  $10^5$  G. Thus the simple result presented above does not apply for the detection scheme used in the Brossel-Bitter experiment and equation (16.20) must therefore be modified. The magnetic dipole transition probabilities for a system with a multiplicity of equally spaced levels have been calculated quantum mechanically by Majorana (1932) and Rabi (1932). However, we prefer to return to our classical model in which the excited atoms are represented as electric dipole oscillators. When  $\pi$ -polarized excitation is used, as in the Brossel-Bitter experiment, the axes of the dipoles at the instant of excitation are parallel to the z-direction. Under the combined influence of the static and rotating magnetic

fields these dipoles precess until after a time interval  $(t-t_0)$  they are inclined at the angle  $\alpha$  to the z-axis, where  $\cos\alpha$  is given by equation (16.12). The  $\sigma$ -polarized resonance fluorescence signal observed in the direction of the magnetic field (see Fig. 16.1) is proportional to the square of the component of the electric dipole moment perpendicular to  $\mathbf{B}$ , giving

$$\begin{aligned}
 I(t, t_0) &= I_0 \sin^2 \alpha \exp\{-\Gamma(t-t_0)\} \\
 &= 2I_0 \sin^2 \beta \left[ \left(1 - \frac{3}{4} \sin^2 \beta\right) - \cos^2 \beta \cos^2 \omega_e(t-t_0)^2 - \right. \\
 &\quad \left. - \frac{1}{4} \sin^2 \beta \cos^2 2\omega_e(t-t_0) \right] \exp\{-\Gamma(t-t_0)\}. \tag{16.22}
 \end{aligned}$$

The signal observed in a steady state experiment is obtained by integrating equation (16.22) from  $t_0 = -\infty$  to  $t$ ; after some manipulation we obtain (Problem 16.4)

$$\begin{aligned}
 I &= \frac{RI_0}{4\Gamma} \sin^2 \beta \left\{ \left(1 - \frac{3}{4} \sin^2 \beta\right) - \frac{\Gamma^2 \cos^2 \beta}{\Gamma^2 + \omega_e^2} - \frac{\Gamma^2 \sin^2 \beta}{4(\Gamma^2 + 4\omega_e^2)} \right\} - \\
 &= \frac{RI_0}{4\Gamma} \frac{\omega_1^2}{\omega_1^2 + (\omega_L - \omega_0)^2} \left\{ \frac{\omega_1^2}{\Gamma^2 + 4\omega_1^2 + 4(\omega_L - \omega_0)^2} + \frac{(\omega_L - \omega_0)^2}{\Gamma^2 + \omega_1^2 + (\omega_L - \omega_0)^2} \right\}. \tag{16.23}
 \end{aligned}$$

In the original experiments of Brossel and Bitter (1952) this expression was checked by determining the values of  $RI_0$  and  $\omega_1$  which fitted the experimental data at resonance and then plotting equation (16.23) using a value for  $\Gamma$  which was obtained by a method described below. As may be seen from Fig. 16.2 there is excellent agreement between the theoretical curves and the experimental points over the entire range of values of both static and r.f. field strengths. When  $\omega_1 = \gamma B_1 \ll \Gamma$  the curves are bell shaped with a maximum at  $B_0 = \omega_0/\gamma$ . As the strength of the rotating field is increased, the amplitude of the resonance signal grows rapidly, as we see in Fig. 16.2. Eventually, when the condition  $\omega_1 \gg \Gamma$  is approached, the second term in equation

(16.23) becomes important and the signal becomes double peaked. This can be regarded as the effect of saturation of the magnetic resonance which occurs when the rotating field  $B_1$  is sufficiently strong that the induced magnetic dipole transitions substantially change the populations of the levels within the excited state lifetime of  $1/\Gamma$ .

### *16.3. Discussion of the optical double-resonance method*

16.3.1. The effects of hyperfine structure. In their original investigation Brossel and Bitter (1952) also performed double-resonance experiments on the odd mercury isotopes  $^{199}\text{Hg}$  and  $^{201}\text{Hg}$  which have nuclear spin  $I=1/2$  and  $3/2$  respectively. The r.f. magnetic field now induces transitions between the hyperfine structure levels  $|F, M_F\rangle$  which satisfy the selection rule  $\Delta F=0$ ,  $\Delta M_F = \pm 1$ . In low magnetic fields the observed resonances allow the  $g_F$  factor (equation (15.28)) of a given hyperfine level to be determined and so lead to a determination of the nuclear spin  $I$  (Problem 16.5).

In addition to these Zeeman resonances, however, r.f. transitions satisfying the selection rule  $\Delta F = \pm 1$ ,  $\Delta M_F = \pm 1$  can also be detected and enable the hyperfine structure intervals in zero field to be obtained. Indeed the investigation of the hyperfine structure of excited energy levels has been one of the main applications of the optical double-resonance technique. However, we reserve a detailed discussion of these experiments until Chapter 18 when the hyperfine structure experiments on both excited and ground state atoms will be considered.

16.3.2. Comparison with the Zeeman effect in optical spectroscopy. In optical double-resonance experiments the Doppler shift due to the motion of an atom through the r.f. magnetic field is negligible in comparison with the natural width of the excited levels. Substituting into equation (16.21) a typical atomic lifetime of  $10^{-7}$  s leads to a linewidth for the magnetic resonance signal, at low r.f. power of

3 MHz. If the centre of this resonance can be determined to 1/100th part of the linewidth and the r.f. field employed has a frequency of 150 MHz, we achieve an accuracy 0.02 per cent in the measurement of  $g_J$ . Although this precision is poor compared with that attainable in atomic beam experiments on ground or long-lived metastable states, it is nevertheless orders of magnitude better than that obtained when using the techniques of optical spectroscopy (Problem 16.6).

The disadvantage, however, of the optical double-resonance method is that the excited levels can only be investigated one by one, and often only a few levels in any given atom can be excited sufficiently strongly to enable accurate measurements to be made. This should be contrasted with the optical Zeeman effect experiments in which a great deal of information about many different spectral lines can be recorded simultaneously by combining a conventional spectrograph and a Fabry-Perot étalon.

16.3.3. Sensitivity of optical double-resonance experiments. In conventional solid state magnetic resonance experiments the necessary population difference between the states is created by the Boltzmann factor  $\exp(\mu B/kT)$  and is enhanced by working at low temperatures and high field strengths. The resonance is detected by changes in the bulk magnetization of the sample or in the radio frequency power absorbed. These factors together limit the sensitivity of the method and samples containing  $10^{12}$  spins per cubic centimetre are required in electron resonance experiments.

By contrast optical double-resonance experiments can be performed with vapour densities as low as  $10^6$  atoms  $\text{cm}^{-3}$ . This great increase in sensitivity is due to the high atomic polarization achieved by optical excitation combined with the fact that in these experiments the absorption of an r.f. quantum triggers the detection of a visible or ultraviolet quantum whose energy is some  $10^6 - 10^7$  times greater. Optical double-resonance experiments can therefore be performed on samples containing only a few milligrams of mass-separated isotopes or even on short-lived radioactive isotopes.

## Optical pumping experiments

### 17.1. Introduction

The success of the Hanle effect and optical double resonance experiments as a means of investigating the lifetimes, energy levels, and collisional processes involving excited atoms raises the interesting question: Can similar techniques be applied to a study of free atoms in the ground state? A way of achieving this, now known as *optical pumping*, was proposed by Kastler (1950), although the first experimental demonstrations of the optical pumping and optical double-resonance methods were not published until 1952. Professor Kastler was awarded the Nobel Prize in 1966 for his seminal contributions to both of these fields.

Optical pumping, then, is a method for producing significant changes in the population distributions of atoms by means of irradiation with light. The term, as used in this chapter, refers to changes in the relative populations of either Zeeman or hyperfine levels belonging to the ground or metastable states of an atom. These changes can be monitored by the modification of the intensity of polarization of the resonantly scattered light, as in optical double-resonance experiments, or more directly by means of the change in intensity of the light transmitted through the optically-pumped sample.

The optical pumping technique permits the investigation of ground-state Zeeman intervals using magnetic resonance methods and many g-factors have been determined to high precision. From the width of the magnetic resonance signals and from the decay rate of transient signals the transverse and longitudinal relaxation times,  $T_2$  and  $T_1$  respectively, can be evaluated and mechanisms for the collisional relaxation elucidated. In low-pressure systems the relaxation occurs principally at the walls of the optical pumping cell and thus a study of the relaxation has increased our under-

standing of surface physics. Optical pumping magnetic resonance signals can be very narrow and this fact has allowed a systematic study to be made of the interactions of atoms with electromagnetic fields in the optical and radio frequency range. This has led to the discovery of shifts in atomic energy levels produced by light and of multiple quantum transitions.

In this chapter we shall be concerned mainly with the principles of the technique, the effect of relaxation processes, and magnetic resonance transitions between Zeeman sub-levels. We shall therefore initially describe the experiments in terms of the populations of the ground state sub-levels. The discussion of the effects of phase coherence (Hertzian coherence) and experiments involving transverse pumping is reserved until section 17.8. Moreover the application of optical pumping methods to the investigation of hyperfine intervals and the measurement of nuclear moments is postponed until Chapter 18, as are the applications of this technique in devices such as magnetometers, atomic clocks, and masers.

### 17.2. Principles of optical pumping

17.2.1. Zeeman pumping in pure vapours. The aim of this particular pumping technique is to create a non-thermal distribution of population among the different magnetic sub-levels belonging to the atomic ground state. The basic principle of the technique may be understood by reference to Fig. 17.1(a) which gives details of the energy levels and resonance lines of rubidium. This structure is typical of all the alkalis; however, we have neglected the nuclear spin and the diagram would apply strictly only to the case  $I=0$ , e.g.  $^{40}\text{Ca}^+$ . By absorption of optical resonance radiation in either the  $D_1$  or  $D_2$  lines, the rubidium atoms can be excited to the  $5\ ^2\text{P}_{1/2}$  or  $5\ ^2\text{P}_{3/2}$  levels from which they will decay spontaneously after a mean lifetime of  $\approx 10^{-8}\text{ s}$ .

In an optical pumping experiment, Fig. 17.2, the light from a rubidium lamp is usually passed through a simple

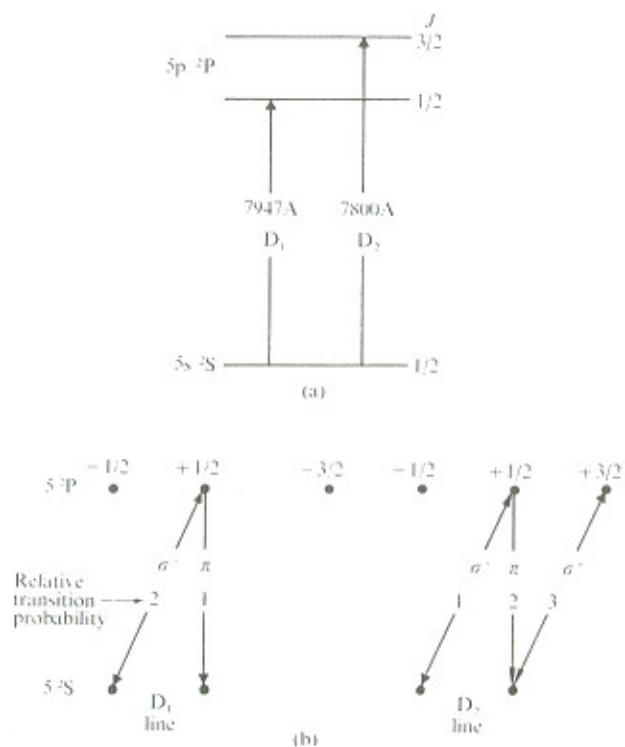


Fig. 17.1. (a) Energy levels and resonance lines of rubidium.  
(b) Zeeman structure of the  $D_1$  and  $D_2$  resonance lines showing the relative transition probabilities of the  $\sigma^+$  and  $\pi$ -polarized components.

interference filter which transmits only the  $D_1$  resonance line. The radiation is then circularly polarized by using a linear polarizer followed by a quarter-wave plate. The light is focussed into a cell which has previously been evacuated and has then had a small quantity of metallic rubidium distilled into it before being sealed off. At room temperature (300 K) the vapour pressure of rubidium ( $\approx 10^{-6}$  Torr) is sufficient to ensure that the sample will initially absorb most of the incident  $D_1$  radiation. A static

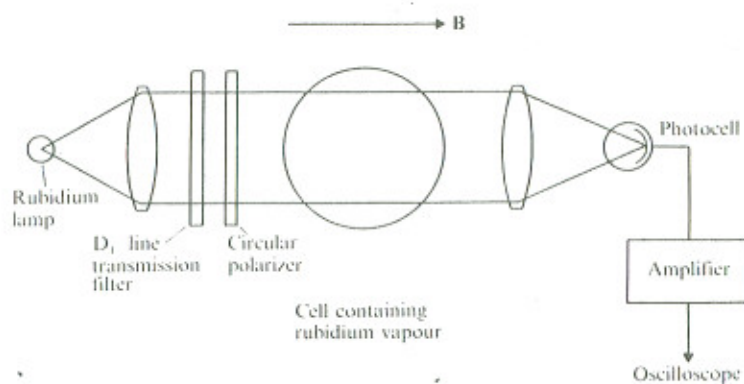


Fig. 17.2. Schematic diagram of the apparatus for a rubidium optical pumping experiment.

magnetic field is applied to the cell in a direction parallel to that of the incident light.

We now recall the selection rules for the Zeeman components of an electric dipole transition:

$$\Delta m = m' - m'' = 0, \pm 1$$

where  $m'$  and  $m''$  are the magnetic quantum numbers of the upper and lower Zeeman states respectively. The selection rule  $\Delta m = +1$  corresponds to the absorption of  $\sigma^+$ -polarized light. For this polarization the sense of rotation of the electric vector is the same as that of an electric current in the Helmholtz coils which generate the magnetic field. An observer looking towards the lamp from the position of the detector in Fig. 17.2 would see the electric vector of  $\sigma^+$  circularly-polarized light rotating in the anti-clockwise sense and would call it left circularly-polarized radiation.

From Fig. 17.1(b) we see that when the atoms in the cell are illuminated with  $\sigma^+$ -polarized  $D_1$  radiation, only those atoms in the  $m_J = -\frac{1}{2}$  state of the ground level can absorb

a photon. These atoms are excited to the  $m_J = +\frac{1}{2}$  state of the  $5^2P_{1/2}$  level where they spend an average lifetime of  $2.8 \times 10^{-8}$  s before spontaneous decay. Two possible decay routes exist:

- (a) back to the  $m_J = -\frac{1}{2}$  state with the re-emission of  $\sigma^+$  polarized light, and
- (b) down to the  $m_J = +\frac{1}{2}$  state with the emission of  $\pi^-$  polarized light.

The transition probabilities for these two decay routes are in the ratio of 2:1. Thus after they have experienced one cycle of absorption and radiative decay, one third of the atoms which were originally in the  $m_J = -\frac{1}{2}$  state end up in the  $m_J = +\frac{1}{2}$  state of the ground level.

The atoms have therefore been optically pumped from a lower to a higher  $m_J$  state. Simultaneously the  $z$ -component of the angular momentum of the atomic system ( $J_z$ ), has been increased. This additional angular momentum has been transferred from the pumping beam to the atomic sample by the absorption of  $\sigma^+$ -polarized photons, each of which possess an angular momentum component of  $+1\hbar$  along the direction of propagation. The random initial orientations of the atomic magnetic moments are therefore altered by the pumping process and the sample acquires a net magnetization. The sample is said to be oriented or polarized by the pumping process. Clearly changing the pumping light to  $\sigma^-$ -polarization will create an atomic polarization in the reverse direction.

This type of optical pumping which results in a sample possessing a non-thermal distribution of population among the sub-levels of the atomic ground state should be distinguished from the flash lamp pumping used in solid state and liquid lasers. In those systems the aim is to transfer a large fraction of the ions or molecules into a different electronic level.

As Fig. 17.1(b) shows,  $\sigma^+$ -polarized  $D_2$  radiation may also be used for optical pumping, the Zeeman component  $m_J = -\frac{1}{2} + m_J = +\frac{1}{2}$  being the effective transition. Although

absorption also occurs in the  $m_J = +\frac{1}{2} + m_J = +\frac{3}{2}$  component this has no effect on the orientation process. Starting from equal populations in the  $m_J = \pm \frac{1}{2}$  levels, the  $D_2$  line will transfer two thirds of the atoms from the lower to the upper state after one pumping cycle. When both  $D_1$  and  $D_2$  lines are used together the optical pumping effect is additive provided that the atoms are not subjected to collisional perturbations whilst in the excited level. We consider the effect of such collisions in the following paragraph.

17.2.2. Zeeman pumping in the presence of a buffer gas. In an evacuated cell atoms of the vapour travel to the cell walls in a time of the order of  $10^{-4}$  s and there the orientation is destroyed. This short effective lifetime of ground state atoms makes it difficult to attain high atomic polarizations and a foreign gas is often added to the optical pumping cell to slow down this relaxation. Most of the atoms on which optical pumping experiments have been performed have ground electronic states with zero orbital angular momentum (e.g. the  $^2S_{1/2}$  states of alkalis and the  $^1S_0$  states of group IIB metals). The wavefunctions of these states are spherically symmetric and the atoms are relatively insensitive to collisions. For these atoms diamagnetic gases such as  $H_2$ ,  $N_2$ , and the noble gases act as 'buffer gases'. The interatomic collisions not only preserve the orientation of the ground state but also prevent the atoms from colliding with the walls of the cell.

Unfortunately collisions also occur between the excited atoms and those of the added gas and at sufficiently high pressure the mean free time between collisions becomes smaller than the radiative lifetime of the excited atoms. Most atoms then undergo collisions before they return to the ground state and the effect of these collisions is to induce transitions between the Zeeman levels of the excited state. As a result of this mixing the emitted resonance fluorescence is partially depolarized, a phenomenon that we discussed in detail in section 16.5.4.

If the foreign gas pressure is very high the excited

atoms will be uniformly distributed among the Zeeman states of the excited level and atoms will then return at the same rate to all states of the ground level. In this extreme the efficiency of the optical pumping process depends only on the rate at which the incident radiation is absorbed by the different ground state Zeeman levels. We consider again the case of an alkali atom illuminated with  $\sigma^+$ -polarized light. If self-absorption in the lamp causes the intensities of the  $D_1$  and  $D_2$  lines to be equal, then both the  $m_J = \pm \frac{1}{2}$  states of the ground level will be emptied at the same rate. This can be verified from Fig.17.1(b) by adding the transition probabilities for the  $D_1$  and  $D_2$  lines. Under these conditions optical pumping can only become efficient if the  $D_2$  radiation is suppressed with a suitable filter. Then only atoms in the  $m_J = -\frac{1}{2}$  state will be excited and an orientation of the sample will be achieved as before. We see therefore that optical orientation can be achieved both with and without a buffer gas but that the illumination conditions must be carefully chosen in each case to ensure the optimum efficiency for the pumping process.

#### 17.2.3. Detection of atomic orientation - transmission

monitoring. When either the  $D_1$  or the  $D_2$  line is used on its own, the discussion of section 17.2.1 shows that a high atomic polarization can be attained after all the atoms in the  $m_J = -\frac{1}{2}$  state have undergone a single optical pumping cycle. If  $N_{\pm}$  are the number densities of atoms in the  $m_J = \pm \frac{1}{2}$  states, the polarization is defined by

$$\text{Polarization} = P = \frac{N_+ - N_-}{N_+ + N_-}. \quad (17.1)$$

From Fig.17.1(b) we deduce that after one cycle the polarization would equal either  $\frac{1}{3}$  or  $\frac{2}{3}$ , depending on whether the  $D_1$  or the  $D_2$  line was used for pumping. As the pumping process continues the cycle is repeated for those atoms left in the  $m_J = -\frac{1}{2}$  state and in the absence of relaxation processes all the atoms would eventually be pumped into the  $m_J = +\frac{1}{2}$  state. When this situation is reached the sample

is no longer able to absorb  $\sigma^+$ -polarized radiation. Thus during the process of orientation, the transparency of the sample to the  $\sigma^+$ -polarized  $D_1$  line increases and the intensity of light transmitted through the cell is directly related to the atomic polarization. A simple photocell followed by an amplifier can be used to monitor the progress of the optical pumping, as shown in Fig.17.2. By the use of phase-sensitive detection the signal-to-noise ratio can be improved and changes of the order of 1 part in  $10^4$  of the transmitted light intensity can be detected.

#### 17.2.4. Detection of atomic orientation - fluorescence

monitoring. An alternative method of monitoring the optical pumping process involves the detection of the fluorescent light emitted by the optically excited atoms in the cell. When the orientation of the sample is complete  $\sigma^+$ -polarized  $D_1$  radiation cannot be absorbed and consequently the atoms no longer re-radiate fluorescent light. Thus the intensity of the fluorescent light directly monitors the population of atoms in the  $m_J = -\frac{1}{2}$  level. The polarization of the fluorescent light in this case is constant although generally it too can be used to monitor the orientation. However, when a high pressure of buffer gas is used in the cell, collisions will equalize the populations of the Zeeman levels of the excited state and the polarization technique will no longer be applicable.

Finally it should be noted that when the sample is pumped by the  $D_1$  and  $D_2$  lines simultaneously, the absorption of the  $D_2$  line becomes stronger as the sample orientation increases. Thus in both the transmission and the fluorescence monitoring schemes the sign and magnitude of the signal obtained when radiation in the  $D_1$  and  $D_2$  lines falls on the detector cannot be simply related to the polarization of the sample. It is therefore again desirable to filter out the  $D_2$  component.

17.2.5. Optical pumping in mercury. In order to widen the scope of our discussion of optical pumping experiments, we

recall that mercury has a high vapour pressure at room temperature. It is therefore a very convenient element for optical pumping experiments, especially when the  $6^1S_0 - 6^3P_1$  intercombination line at  $2537 \text{ \AA}$  is used. We are now of course only concerned with the odd mercury isotopes  $^{199}\text{Hg}$  and  $^{201}\text{Hg}$  which have nuclear spins of  $I = \frac{1}{2}$  and  $I = \frac{3}{2}$  respectively. To improve the efficiency of the optical pumping cycle it is again desirable to be able to isolate different components of the resonance line. Although the hyperfine structure cannot be resolved by anything as simple as an interference filter, nevertheless the use of separated isotopes in the resonance lamps enables the necessary selection to be obtained. Thus by using  $^{204}\text{Hg}$  in the lamp and  $^{199}\text{Hg}$  in the cell it is possible to pump on the component connecting the  $6^1S_0 (I=\frac{1}{2})$  ground state with the  $6^3P_1 (F=\frac{1}{2})$  level only. The pumping scheme is then identical to the pumping of alkali atoms using filtered D<sub>1</sub> radiation and much of our preceding discussion applies equally to the experiments on mercury.

There are, however, two very important differences: first the spin angular momentum of the ground state atoms is now associated with a nuclear magnetic moment rather than with an electron moment. Consequently the relaxation time for the nuclear spins is very much longer than that of the electron spins and optical pumping experiments in mercury ought to be easier than those in alkali vapours. Secondly, however, the transition probability for the  $2537 \text{ \AA}$  line, is a factor of ten smaller than those of the resonance lines of the alkalis. This means that the time constant for nuclear orientation by optical pumping in mercury is rather long and indeed many of the initial experiments failed because of the low intensities of the available sources of  $2537 \text{ \AA}$  radiation. The first successful experiments were reported by Cagnac (1958) using intense microwave lamps. This pioneering work is described in more detail in his thesis (Cagnac 1961).

The isotope  $^{199}\text{Hg}$  has only two ground state magnetic sub-levels and so has served as an important test case for the basic theory of optical pumping, developed in more detail

in sections 17.8 and 17.9. Many detailed comparisons between the theory and experiments using this isotope can be found in another outstanding thesis from the Paris group (Cohen-Tannoudji 1962). Although in  $^{201}\text{Hg}$  the ground state has four magnetic sub-levels, it is still true that by illuminating the cell with  $\sigma^+$ -polarized radiation from a  $^{204}\text{Hg}$  lamp, the atoms will be concentrated in the states of higher  $M_I$  quantum numbers and the sample acquires a net magnetic moment. In this case the ground state nuclear spins are said to be oriented. However, if the cell is illuminated with unpolarized light travelling along the direction of the field  $B$  both  $\sigma^+$  and  $\sigma^-$  components are absorbed with equal probability. The ground state sub-levels with large values of  $|M_I|$  are then filled at the expense of those with small values of  $|M_I|$ . Although the sample now has no net magnetic moment, it does have a non-thermal distribution of population and is said to be aligned. When we do not wish to distinguish between orientation and alignment we shall say that the sample is polarized.

### 17.3. Effect of relaxation processes

17.3.1. Conditions to be fulfilled for efficient pumping. The state of complete polarization is, of course, never attained experimentally since relaxation processes tend to restore the spin distribution to thermal equilibrium. In a given experimental situation one relaxation process is generally dominant and can be characterized by a definite longitudinal relaxation time  $T_1$ . When the pumping light is suddenly interrupted, for instance by a shutter, the rate of change of the population difference,  $n = N_+ - N_-$ , obeys the equation

$$\left[ \frac{dn}{dt} \right]_{\text{relax}} = -n/T_1. \quad (17.2)$$

Since the net magnetic moment per unit volume of the system is given by

$$\langle M_z \rangle = |\mu| (N_+ - N_-) \quad (17.3)$$

where  $|\mu| = g_J \mu_B J$  is the magnetic moment of an atom with total angular momentum  $J$ , it will decay exponentially with the time constant  $T_1$ :

$$\langle M_z(t) \rangle = \langle M_z(0) \rangle \exp(-t/T_1). \quad (17.4)$$

For completeness we note that the magnetization  $\langle M_z \rangle$  and the degree of polarization defined by equation (17.1) are proportional to one another, being related by

$$P = \frac{N_+ - N_-}{N} = \frac{\langle M_z \rangle}{|\mu| N} \quad (17.5)$$

where  $N$  is the total number density of atoms in the sample.

The longitudinal relaxation which takes place in the dark is obviously also present when the cell is illuminated with pumping radiation. However, we must now take into account the transitions stimulated by the absorption of light. The net rate at which atoms are pumped from the  $m_J = -\frac{1}{2}$  state to the  $m_J = +\frac{1}{2}$  state is given by

$$dN_+ = -dN_- = \alpha P_{\mu m} N_- dt \quad (17.6)$$

where  $P_{\mu m}$  is the absorption probability for electric dipole transitions given by equation (9.40) and  $\alpha$  is a numerical factor less than unity which accounts for the fact that only a certain fraction of the excited atoms decay to the  $m_J = +\frac{1}{2}$  state. Noting that  $N_- = (N-n)/2$  and that the absorption probability is proportional to the intensity of the incident light,  $I$ , we find that

$$\left[ \frac{dn}{dt} \right]_{\text{pump}} = K' I (N-n) \quad (17.7)$$

where  $K'$  is a constant. Introducing the pumping time constant  $T_p' = 1/K'I$ , the total rate of change of the difference in population densities under the simultaneous action of both the pumping and the relaxation processes becomes

$$\frac{dn}{dt} = \frac{N-n}{T_p'} - \frac{n}{T_1}. \quad (17.8)$$

Thus the approach to the equilibrium polarization is described by the equation (Problem 17.1):

$$\frac{n(t)}{N} = P(t) = P(\infty) (1 - \exp(-t/\tau_1)) \quad (17.9)$$

where

$$1/\tau_1 = 1/T_p' + 1/T_1, \quad (17.10)$$

and  $P(\infty)$  is the steady state polarization given by

$$P(\infty) = (1 + T_p'/T_1)^{-1}. \quad (17.11)$$

We see that to obtain a large steady state polarization we must satisfy the condition  $T_p' \leq T_1$ , i.e. the pumping rate must be faster than the relaxation rate. Although this condition could have been derived intuitively, the equations developed above will be useful in the subsequent discussion of the experimental determinations of the longitudinal relaxation time  $T_1$ .

17.3.2. Light sources for optical pumping. Obviously for a high pumping rate an intense source of resonance radiation is required. With ordinary commercial lamps pumping times of the order of  $10^{-3}$  s can be obtained, but substantial improvements can be made by using small electrodeless lamps which are excited by microwave or high radio frequency power (Problem 17.2). To avoid self-reversal of the resonance lines the lamps are made in the form of a thin disk or a re-entrant sphere as shown in Fig. 17.3. The lamps are thoroughly baked under vacuum before being filled with a small quantity of metal and approximately 1 Torr of noble gas, usually argon, to carry the discharge while the lamp is warming up. Because the quantity of metal that is required for these lamps is very small ( $\approx 5$  mg), they are very convenient when using pure isotopes.

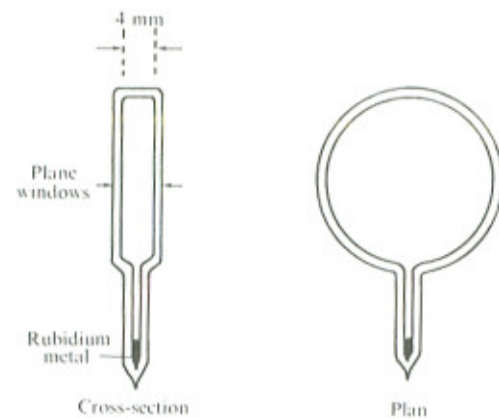


Fig. 17.3. Electrodeless lamp for optical pumping experiments in alkali metal vapours.

17.3.3. Optical pumping cells. In order to attain strong steady state polarization it is also necessary to make the relaxation as slow as possible. The first optical pumping experiments of Brossel *et al.* (1952) and Hawkins and Dicke (1953) were made on atomic beams of sodium where relaxation is absent. However, the rapid flight of the atoms through the pumping region severely limited the time that the atoms were illuminated. It was later realized that the experiments could be performed more simply by using low density atomic vapours in sealed-off cells. The relaxation time is then the mean time between two wall collisions and is of the order of  $10^{-4}$  s for a spherical cell having a diameter of 5 cm (Problem 17.3). This relaxation time can be increased considerably either by filling the cell with a suitable buffer gas or by coating the walls of the cell with certain hydrocarbon films. These techniques will be discussed in more detail in the following section.

#### 17.4. Investigation of longitudinal relaxation times

##### 17.4.1. Experimental technique.

A convenient method for the

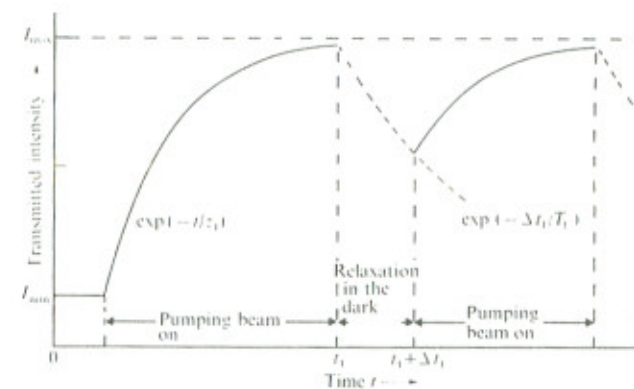


Fig. 17.4. The time dependence of the intensity of light transmitted through an optically-pumped atomic vapour.

measurement of longitudinal relaxation times was introduced by Franzen (1959) in a study of the effect of different buffer gases on the efficiency of the optical pumping cycle. The principle of this technique may be understood by reference to Fig. 17.4, which shows the signal observed in a transmission monitoring experiment. At time  $t=0$  the optical pumping lamp is switched on but, because there are initially equal numbers of atoms in the  $m_J = \pm \frac{1}{2}$  states, the vapour is absorbing and the transmitted intensity is low. The transparency of the vapour increases with time as the pumping proceeds and the signal approaches its maximum value with the exponential time constant  $t_1$  given by equation (17.10). At some later time  $t_1$ , a shutter is inserted to cut off the pumping beam and the atoms of the vapour start to relax in the dark with a time constant  $T_1$ , as described by equation (17.4). Thus when the shutter is re-opened at time  $t_1 + \Delta t_1$ , the transparency of the vapour has been reduced below its maximum value and the transient optical pumping signal starts again from a point lying between  $I_{\max}$  and  $I_{\min}$ .

The exponential curve governing the relaxation in the dark can be mapped out by superimposing the signals corresponding to a series of different time intervals  $\Delta t_1$  on a single oscilloscope photograph. This is illustrated

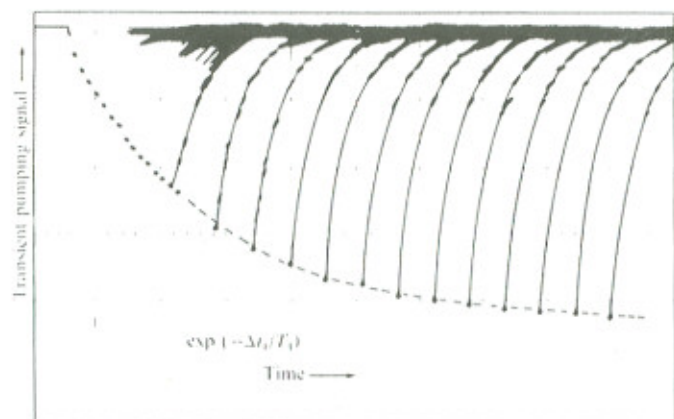


Fig.17.5. Oscillogram showing the longitudinal relaxation of  $^{87}\text{Rb}$  vapour observed by Gibbs and Hull (1966). The transients result from reopening the shutter after different time intervals spent relaxing in the dark and show the approach to optical pumping equilibrium. The bright spots from which each trace begins plot out the decay curve,  $\exp(-\Delta t_1/T_1)$ .

in Fig.17.5 for the relaxation in a  $^{87}\text{Rb}$  cell observed by Gibbs and Hull (1966). The starting points of the transient signals lie on the curve

$$I(\Delta t_1) = I_{\min} + (I_{\max} - I_{\min}) \exp(-\Delta t_1/T_1)$$

and a detailed analysis enables the longitudinal relaxation time  $T_1$  to be determined. Once the value of  $T_1$  has been measured, the pumping time  $T_p'$  for a given light intensity can be obtained by analysis of the transient signals obtained when the cell is illuminated.

## The hyperfine structure of atoms and its investigation by magnetic resonance methods

When an optical spectral line is isolated and examined under high resolution it is usually found to consist of a partially resolved blend of many different components lying within  $10^{-3}$  -  $1 \text{ cm}^{-1}$  of the line centre. This complex of components is generally the result of two quite different effects: isotope shift and hyperfine structure. As we have already noted several times in Chapters 15-17, the centres of gravity of the spectral lines emitted by different isotopes are displaced from one another by the effect of the different masses and charge distributions of their nuclei. Although isotope shifts contain valuable information about some properties of the atomic nucleus, measurements of these shifts by magnetic resonance techniques are impossible because the energy levels involved belong to two quite distinct atoms. We shall therefore not discuss isotope shifts any further but refer the reader to the review article by Stacey (1966) for additional information. The effect can be eliminated when it is experimentally undesirable by using a source containing a single pure isotope of the element of interest.

On the other hand when the spectra of each of the odd isotopes of an element are examined in detail, it is found that there is a residual structure known as the *hyperfine structure*. Pauli (1924) suggested that this was due to a magnetic moment  $\mu_1$  associated with an intrinsic nuclear spin angular momentum of  $\hbar I$ . The interaction of the magnetic moment of the nucleus with the magnetic field produced by the valence electrons causes a small splitting of the energy levels of an atom and provides the largest contribution to the observed hyperfine structure.

The small scale of the hyperfine splittings and the large Doppler width of spectral lines makes accurate measurements by optical spectroscopy very difficult. Mag-

netic dipole transitions, however, can be induced directly between the different hyperfine-structure levels of a given configuration and the precision of the measurements by radio-frequency spectroscopy is then generally limited only by the natural width of the energy levels involved. This precision can be extremely high for the ground states and long-lived metastable states of free atoms, as we saw in Chapter 17.

Magnetic resonance measurements on both ground state and excited levels of atoms yield values of the nuclear spin, the nuclear magnetic moment, and of the nuclear electric quadrupole moment. In this chapter we shall discuss the investigation of the hyperfine structure of atoms by the optical pumping, atomic beam, and optical double-resonance techniques. Although the data obtained are of fundamental interest, the application of these techniques to the construction of atomic clocks and maser oscillators is perhaps of more practical importance. Before moving on to the discussion of these topics, we briefly outline the basic theory of atomic hyperfine structure and the associated Zeeman effect closely following the more detailed account given in Woodgate (1970).

### 18.1. Theory of hyperfine structure

18.1.1. Magnetic dipole interaction. We consider first the interaction of the nuclear magnetic moment  $\mu_I$  with the magnetic field  $B_{el}(0)$  produced at the nucleus by the valence electrons. Consideration of the classical energy of orientation in the field allows the Hamiltonian describing the interaction to be written in the form:

$$\mathcal{H}_1 = -\mu_I \cdot B_{el}(0). \quad (18.1)$$

We assume that this term can be treated as a small perturbation when compared with the zeroth-order Hamiltonian,  $\mathcal{H}_0$ , which describes the central electrostatic field of the atom, the repulsion between electrons, and the spin-orbit interaction. We need therefore only consider the effect of  $\mathcal{H}_1$  on the states labelled by the quantum numbers ( $\gamma$  LSJ). It

follows that  $J$  and  $I$  are good quantum numbers and that the nuclear magnetic moment may be written in the form

$$\mu_I = g_I \mu_n I \quad (18.2)$$

where  $g_I$  is the nuclear g-factor and  $\mu_n = e\hbar/2M$  is the nuclear magneton which depends on the proton mass,  $M$ . The nuclear magnetic moment of the atom,  $\mu_I$ , is defined as the largest observable component of  $\mu_I$ :

$$\mu_I = \langle I, M_I=I | \mu_z | I, M_I=I \rangle = g_I \mu_n I.$$

Two points should be noted in connection with equation (18.2): firstly, the sign adopted in this equation differs from that of the corresponding equation (5.85) for electronic magnetic moments because the nucleus is positively charged; and secondly, nuclear magnetic moments are typically two thousand times smaller than atomic magnetic moments since  $\mu_n/\mu_B = m/M \approx 1/1836$ . The nuclear g-factor, which is of the order of unity, takes account of the way the resultant nuclear moment is built up from the magnetic moments of individual nucleons. It therefore contains information about the detailed internal structure of the nucleus.

Since the magnetic field at the nucleus,  $B_{el}(0)$ , is determined by the motion of the atomic electrons it follows that equation (18.1) may be rewritten as

$$\mathcal{H}_1 = A_J I \cdot J \quad (18.3)$$

where  $A_J$  is called the magnetic hyperfine structure constant and is the quantity which is determined directly from experimental measurements. For a hydrogenic atom, or an atom with just one electron outside closed shells,  $B_{el}(0)$  and  $J$  are antiparallel and the constant  $A_J$  will be positive if the nucleus has a positive value of  $g_I$ . The magnetic field at the nucleus will be zero for atoms with closed sub-shells and will be largest for those atoms with electrons in penetrating orbits. We would therefore expect to observe the largest hyperfine splitting in atoms with unpaired s-electrons,

e.g. hydrogen and the alkalis.

It can be shown that, of the possible higher-order multipole moments, the nuclear magnetic moments of even order vanish because of symmetry requirements with respect to the nuclear equatorial plane. The next non-vanishing moment, the nuclear magnetic octupole moment, is very small and will be ignored here.

**18.1.2. Electric quadrupole interaction.** Although the magnetic dipole interaction is responsible for the largest contribution to the observed hyperfine structure, the finite extent of the nuclear electric charge distribution is also significant in many cases. We therefore consider the electrostatic interaction between a proton at the point  $\underline{r}_n$  and an electron at the point  $\underline{r}_e$ , given by

$$\mathcal{H}_2 = -\frac{e^2}{4\pi\epsilon_0 |\underline{r}_e - \underline{r}_n|} \quad (18.4)$$

where the origin is taken as the centre of mass of the nucleus. To account for the finite extent of the nuclear charge distribution, we assume  $r_e > r_n$  and expand equation (18.4) in ascending powers of  $r_n/r_e$ , giving

$$\begin{aligned} \mathcal{H}_2 &= -\frac{e^2}{4\pi\epsilon_0} (r_e^2 + r_n^2 - 2r_e r_n \cos\theta_{en})^{-1/2} \\ &= -\frac{e^2}{4\pi\epsilon_0} \sum_k \frac{r_n^k}{r_e^{k+1}} P_k(\cos\theta_{en}) \end{aligned} \quad (18.5)$$

where  $P_k(\cos\theta_{en})$  is the Legendre polynomial of order  $k$  and  $\theta_{en}$  is the angle between  $\underline{r}_e$  and  $\underline{r}_n$  shown in Fig. 18.1.

The first term in the summation of equation (18.5) represents a monopole interaction and when summed over all the protons and electrons gives the familiar Coulomb interaction  $-\sum_i Ze^2/4\pi\epsilon_0 r_{ei}$ . The second term represents a nuclear electric dipole interaction which, by the application of parity and time-reversal symmetry arguments, can be shown to be identically zero, as are the higher electric multipole moments of odd order. Finally the term with  $k=2$  corresponds to an electric quadrupole interaction as we

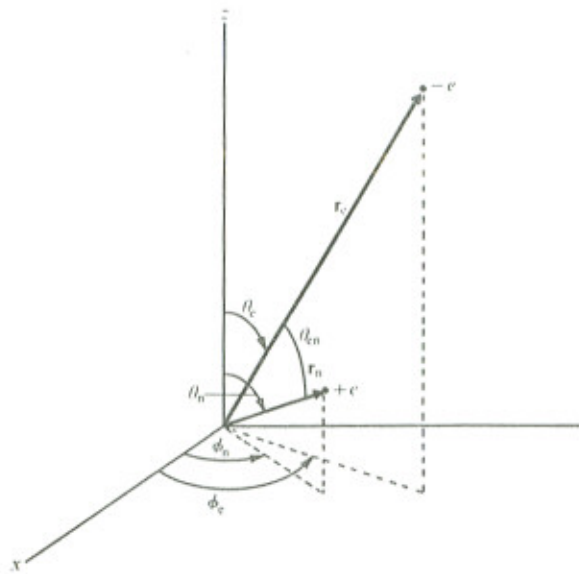


Fig. 18.1. Definition of the angles  $(\theta_n, \phi_n)$  for a proton charge  $+e$  and of  $(\theta_e, \phi_e)$  for an electron of charge  $-e$ , together with the angle  $\theta_{en}$  between  $\underline{r}_e$  and  $\underline{r}_n$ .

shall now demonstrate. We complete the separation of electric and nuclear coordinates in equation (18.5) by applying the spherical harmonic addition theorem:

$$P_k(\cos\theta_{en}) = \frac{4\pi}{2k+1} \sum_{q=-k}^k (-)^q Y_k^q(\theta_n, \phi_n) Y_k^q(\theta_e, \phi_e) \quad (18.6)$$

where  $Y_k^q(\theta, \phi)$  is the  $q^{\text{th}}$  component of the spherical harmonic of order  $k$  and the spherical polar coordinates  $(\theta, \phi)$  are defined with respect to an arbitrary  $z$ -axis fixed in space (see Fig. 18.1). The electric quadrupole interaction then becomes

$$\begin{aligned} \mathcal{H}_2 &= \frac{1}{4\pi\epsilon_0} \sum_{q=-2}^2 (-)^q \left\{ \left(\frac{4\pi}{5}\right)^{1/2} e r_n^2 Y_2^q(\theta_n, \phi_n) \right\} \times \\ &\quad \times \left\{ \left(\frac{4\pi}{5}\right)^{1/2} \left(\frac{-e}{r_e^3}\right) Y_2^q(\theta_e, \phi_e) \right\} \\ &= \frac{1}{4\pi\epsilon_0} \sum_q (-)^q Q_2^q(n) F_2^q(e). \end{aligned} \quad (18.7)$$

When summed over all the protons and electrons, this equation gives the complete nuclear electric quadrupole interaction. We observe that it has the form of the scalar product of a nuclear electric quadrupole tensor and an electric field gradient tensor, each of rank two.

The expression given in equation (18.7) may be simplified by defining the nuclear electric quadrupole moment  $Q$  as

$$\begin{aligned} Q &= \frac{2}{e} \langle I, M_I=I | \sum_j Q_2^0(n_j) | I, M_I=I \rangle \\ &= \langle II | \sum_j r_{nj}^2 (3\cos^2\theta_{nj} - 1) | II \rangle \end{aligned} \quad (18.8)$$

where the summation extends over all the protons in the nucleus (Problem 18.1). In the same way the electronic part of equation (18.7) may be simplified by introducing the average field gradient at the nucleus defined by

$$\begin{aligned} \left( \frac{\partial^2 V_e}{\partial z^2} \right) &= \frac{2}{4\pi\epsilon_0} \langle JJ | \sum_i F_2^0(e_i) | JJ \rangle \\ &= - \langle JJ | \sum_i \frac{e(3\cos^2\theta_{ei} - 1)}{4\pi\epsilon_0 r_{ei}^3} | JJ \rangle \end{aligned} \quad (18.9)$$

where the summation is now over the valence electrons of the atom. Using equation (18.8) and (18.9), it can be shown that the electric quadrupole interaction can be written in the form

$$\mathcal{H}_2 = \frac{B_J}{2I(2I-1)J(2J-1)} \{ 3(\underline{I}, \underline{J})^2 + \frac{3}{2}(\underline{I}, \underline{J}) - I(I+1)J(J+1) \} \quad (18.10)$$

where  $B_J$  is the electric quadrupole interaction constant defined by

$$B_J = eQ \left\langle \frac{\partial^2 V_e}{\partial z^2} \right\rangle. \quad (18.11)$$

Hyperfine structure measurements on free atoms enable the values of  $B_J$  to be determined experimentally. However, the nuclear electric quadrupole moment can then only be calculated if theoretical estimates of the field gradient exist. Since the values of  $\langle \partial^2 V_e / \partial z^2 \rangle$  are seldom known to an accuracy of better than 25 per cent, precise values of the electric quadrupole moments have only been determined in a few special cases. Finally we note that the quadrupole moment  $Q$  is positive if the nuclear charge distribution is elongated along the direction of the nuclear spin  $I$  (prolate) and is negative if the distribution is flattened in this direction (oblate).

18.1.3. Hyperfine structure Hamiltonian. The energy of an atom with finite nuclear spin in a uniform external magnetic field  $B$  is then determined by the sum of the zeroth-order Hamiltonian  $\mathcal{H}_0$  and the hyperfine structure Hamiltonian:

$$\begin{aligned} \mathcal{H}_{\text{HFS}} &= A_J \underline{I}, \underline{J} + \frac{B_J}{2I(2I-1)J(2J-1)} \{ 3(\underline{I}, \underline{J})^2 + \frac{3}{2}(\underline{I}, \underline{J}) - I(I+1)J(J+1) \} + \\ &+ g_J \mu_B \underline{J}, \underline{B} - g_I \mu_N \underline{I}, \underline{B} \end{aligned} \quad (18.12)$$

The third and fourth terms in this equation represent the interaction of the electronic and nuclear magnetic moments with the external magnetic field, the difference in sign arising from the difference in the conventions used in defining  $g_J$  and  $g_I$  as noted above. The interaction constant  $B_J$  is identically zero if  $I=0$  or  $\frac{1}{2}$ , for the nuclear charge distribution is spherically symmetric in these cases: similarly  $B_J$  is also zero if  $J=0$ ,  $\frac{1}{2}$  for then the electron charge distribution is spherically symmetric and  $\langle \partial^2 V_e / \partial z^2 \rangle$  vanishes. It follows that, even when the nucleus possesses a finite quadrupole moment, this cannot be detected by measurements

on the ground states of elements of groups I, II, or III of the periodic table. The information obtained by optical pumping and atomic beam methods is therefore incomplete and this provided one of the major incentives for the development of the optical double-resonance technique, for states with  $J > \frac{1}{2}$  can then be investigated.

18.1.4. Hyperfine structure in zero magnetic field. In the absence of nuclear magnetic dipole or electric quadrupole interactions the zeroth-order wavefunctions  $|\gamma JIM_J M_I\rangle$  are  $(2I+1)(2J+1)$ -fold degenerate in the nuclear and electronic magnetic quantum numbers. To evaluate the energy shift arising from the hyperfine interaction in zero magnetic field, we take linear combinations of the functions  $|\gamma JIM_J M_I\rangle$  to form new zeroth-order wavefunctions  $|\gamma JIFM_F\rangle$  for which the total angular momentum  $F$  and the projection  $M_F = M_J + M_I$  are good quantum numbers. On the vector model the magnetic interaction  $A_J \underline{I} \cdot \underline{J}$  may be imagined to cause  $\underline{I}$  and  $\underline{J}$  to precess rapidly about the resultant total angular momentum

$$\underline{F} = \underline{I} + \underline{J}. \quad (18.13)$$

The energy of a particular hyperfine level is then given by

$$\begin{aligned} E_F &= \langle \gamma JIFM_F | \mathcal{H}_0 + \mathcal{H}_{\text{HFS}} | \gamma JIFM_F \rangle \\ &= E_J + \frac{1}{2} A_J K + \frac{B_J}{8I(2I-1)J(2J-1)} \{ 3K(K+1) - 4I(I+1)J(J+1) \} \end{aligned} \quad (18.14)$$

where  $E_J$  is the energy of the fine-structure multiplet level with total electronic angular momentum quantum number  $J$ , and  $K$  is given by

$$K = F(F+1) - I(I+1) - J(J+1). \quad (18.15)$$

From equation (18.14) we see that the magnetic and electric interaction between the nucleus and the orbital electrons splits a given fine-structure level into a hyper-

fine-structure multiplet. The number of levels produced is equal to the number of possible orientations of the angular momentum vectors  $\underline{I}$  and  $\underline{J}$ , i.e.  $2I+1$  if  $J \geq I$  and  $2J+1$  if  $I \geq J$ . Although the quadrupole term vanishes identically in only a few cases, it has generally been found to be small compared with the magnetic dipole term. Thus, in the limit  $B_J \ll A_J$ , we find that there is an exact analogy between the magnetic interactions giving rise to fine structure on the one hand and hyperfine structure on the other, the quantum numbers  $(L, S, J)$  being replaced by the quantum numbers  $(J, I, F)$  respectively. From equations (18.14) and (18.15) it follows that in the limit  $B_J \ll A_J$  there is a hyperfine-structure interval rule (Problem 18.2):

$$\Delta E = E_F - E_{F-1} = A_J F$$

corresponding to the interval rule for fine structure derived in section 3.9.5.

A consideration of the additional energy shift produced when  $B_J$  is finite shows that each hyperfine level is affected in a different way and this upsets the interval rule. For the case of nuclear spin  $I=3/2$ , which applies to  $\text{Na}^{23}$ ,  $\text{K}^{39}$ ,  $\text{Rb}^{87}$ ,  $\text{Hg}^{201}$  amongst others, the zero-field hyperfine splittings are predicted to have the following values (Problem 18.3):

$$\left. \begin{aligned} J = \frac{1}{2} & \quad E_2 - E_1 = 2A_{1/2} \\ J = \frac{3}{2} & \quad E_3 - E_2 = 3A_{3/2} + B_{3/2} \\ & \quad E_2 - E_1 = 2A_{3/2} - B_{3/2} \\ & \quad E_1 - E_0 = A_{3/2} - B_{3/2} \end{aligned} \right\} \quad (18.16)$$

It follows that in the state  $J=3/2$ , the order of the hyperfine levels depends critically on the sign and magnitude of the ratio  $A_J/B_J$ .

18.1.5. Zeeman effect in weak magnetic field. In magnetic fields of less than  $10^{-3}$  T the condition  $g_J \mu_B B \ll A_J$  is usually

condition requires that the nuclear angular momentum  $J$  and the orbital angular momentum  $L$  be satisfied and the nuclear spin  $I$  and the electronic angular momentum  $J$  remain strongly coupled.<sup>6</sup> However, the third and fourth terms in equation (18.12) introduce an extra energy,  $E_{FM_F}$ , which must be added to that given by equation (18.14). Using the techniques developed in section 3.9.6 we find that

where  $g_p$  is the effective g-value given by

$$g_F = g_J \left\{ \frac{F(F+1) + J(J+1) - I(I+1)}{2F(F+1)} \right\} - g_I \left\{ \frac{F(F+1) + I(I+1) - J(J+1)}{2F(F+1)} \right\} \quad (18.18)$$

and the magnetic quantum number  $M_F$  takes the  $2F+1$  values  $F, F-1, \dots, -F$ . The interaction with the external magnetic field therefore removes the previously existing  $(2F+1)$ -fold degeneracy of each hyperfine level  $|\gamma J M_J\rangle$  and causes the vector  $\mathbf{F}$  to precess about the field direction at the Larmor angular frequency  $\omega_L = g_F \mu_B B / \hbar$ , as shown in Fig. 18.2.

In equation (18.18) the factor  $g_1 m/M$  is three orders of magnitude smaller than  $g_J$  and can often be neglected, especially in experiments involving excited atoms. We are then ignoring the direct interaction of the nuclear magnetic moment with the laboratory field while retaining its interaction with the internal atomic field, the effects of which are described by the first term in equation (18.18).

18.1.6. Zeeman effect in strong magnetic fields. In the Zeeman splitting of fine-structure levels it is rare to find a case in which the applied field is sufficiently large that  $\underline{L}$  and  $\underline{S}$  are completely decoupled and the Paschen-Back effect observed. On the other hand, in hyperfine levels where the largest values of  $A_J/h$  have typical values of 1000 MHz, then a field of only 0.1 T must be considered quite strong. In the high field limit  $g_J \mu_B B \gg A_J$ , the complete hyperfine tensorian is evaluated in the uncoupled representation  $[JIM_1M_1]$ .

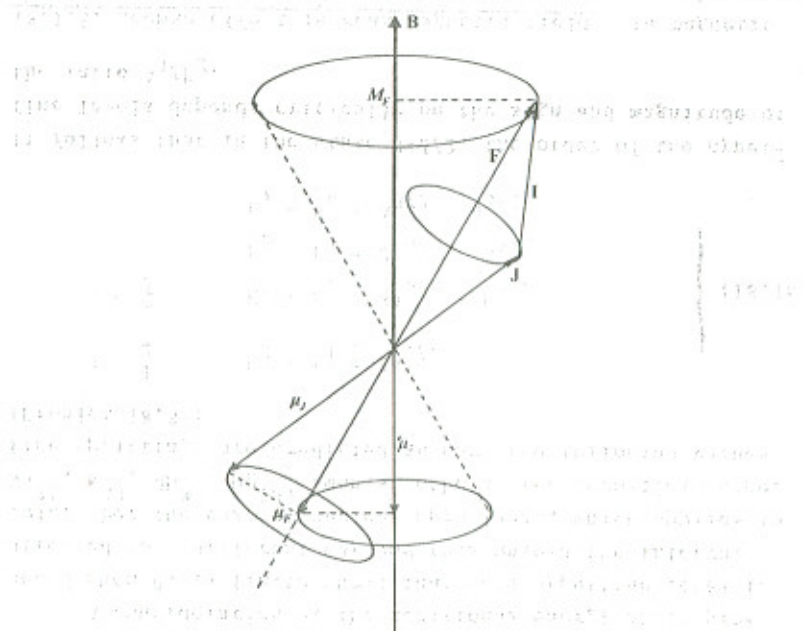


Fig.18.2. Vector model for the atomic magnetic moment  $\mu$

showing the projections first on the direction of  $\vec{F}$  and then on the  $z$ -axis. The interaction between  $\mu_1$  and the external field is neglected.

$$E_{M_J M_I} = g_J \mu_B B M_J - g_I \mu_n B M_I + A_J^* M_J M_I + \frac{B_J}{4I(2I-1)J(2J-1)} (3M_J^2 - J(J+1))(3M_I^2 - I(I+1)). \quad (18.19)$$

The first term in this equation represents the Zeeman splitting of the multiplet level characterized by the quantum number  $J$  while the third term causes each Zeeman sub-level  $M_J$  to be further sub-divided into  $(2I+1)$  hyperfine

Zeeman levels corresponding to the different possible values of  $M_I$ . For any Zeeman level the transition from weak to strong field takes place in such a way that the magnetic quantum number  $M_q$  is preserved. In weak fields  $M_q$  is identical with the quantum number  $M_F$ , and in strong fields we have  $M_q = M_J + M_I$ .

18.1.7. Zeeman effect in intermediate fields. In intermediate fields all the matrix elements of the hyperfine interaction,  $\chi_{HFS}$ , must be evaluated and the energy levels obtained by the solution of the secular equation. For large values of  $I$  and  $J$  this is a task best left to a computer, but if  $I$  or  $J$  does not exceed  $\frac{1}{2}$  then no equation of order higher than quadratic is involved. The solution for  $J=1/2$  and arbitrary values of  $I$  is important because it applies to the  $^2S_{1/2}$  ground states of hydrogen and all the alkalis. The result is the well-known Breit-Rabi formula (Problem 18.4):

$$E_{M_J M_I} = -\frac{\hbar v_{HFS}}{2(2I+1)} - g_I \mu_B M_q \pm \frac{\hbar v_{HFS}}{2} \left\{ 1 + \frac{4M_q x}{2I+1} + x^2 \right\}^{1/2} \quad (18.20)$$

where  $\hbar v_{HFS} = A_J(I + \frac{1}{2})$  is the energy separation between the levels  $F = I \pm \frac{1}{2}$  in zero magnetic field,  $M_q = M_I \pm \frac{1}{2}$ , and the dimensionless parameter  $x$  is given by

$$x = \frac{(g_J + g_I m/M) \mu_B}{\hbar v_{HFS}} \quad . \quad (18.21)$$

In equation (18.20) the plus sign is to be used for states originating from the zero-field hyperfine level  $F=I + \frac{1}{2}$  and the minus sign for states originating from  $F=I - \frac{1}{2}$ . In many ground-state magnetic resonance experiments the precision is such that intermediate coupling and formulae like equation (18.20) provide the only satisfactory basis in which to analyse the observed resonance frequencies.

The quadrupole interaction vanishes for  $J = \frac{1}{2}$  so that the Breit-Rabi formula gives an exact description of the hyperfine structure in this case. If the small term  $g_I \mu_B M_q$  is omitted, a universal plot can be made of  $E_{M_J M_I}$  as a function

of the parameter  $x$ , which is in turn proportional to the applied magnetic field  $B$ . Such a plot is shown in Fig. 18.3 for an atom having  $J = \frac{1}{2}$  and  $I = \frac{3}{2}$  and a further example is shown in Fig. 18.14. The construction of additional diagrams is left as an exercise for the student (Problem 18.5). It

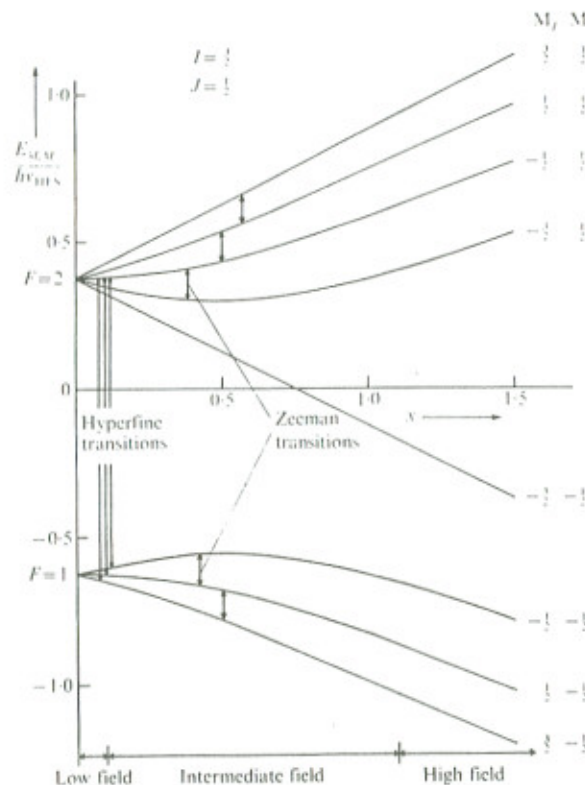


Fig. 18.3. A plot of the Breit-Rabi formula for the case  $I = \frac{3}{2}$ . The abscissa is given by  $x = (g_J + g_I m/M) \mu_B / \hbar v_{HFS}$  where  $\hbar v_{HFS}$  is the energy difference between the levels  $F=2$  and  $F=1$  in zero field.

is useful to remember that  $M_Q$  remains a good quantum number in intermediate fields, states for which  $M_Q = M_F$  in low fields, going over into states with  $M_Q = M_I + M_J$  in strong fields.

18.1.8. Selection rules for magnetic dipole transitions. In the following sections we shall be mainly interested in magnetic dipole transitions induced between the different hyperfine sub-levels by a time-dependent magnetic field  $\underline{B}_1(t)$ . The effect of this field on the atoms may be calculated using the techniques described in section 9.3, provided only that the perturbation operator  $\mathcal{H}_1 = -\underline{p} \cdot \underline{E}(t)$  is replaced by the operator  $\mathcal{H}'_1 = -\underline{\mu} \cdot \underline{B}_1(t)$ . For a magnetic field of amplitude  $B_1$  rotating in the  $x$ - $y$  plane at the angular frequency  $\omega_0$  we have

$$\begin{aligned}\mathcal{H}'_1 &= -\underline{\mu} \cdot (\cos \omega_0 t \hat{i} + \sin \omega_0 t \hat{j}) B_1 \\ &= -\frac{B_1}{2} \{\mu_+ \exp(-i\omega_0 t) + \mu_- \exp(i\omega_0 t)\} \quad (18.22)\end{aligned}$$

where  $\mu_{\pm} = \mu_x \pm i\mu_y$ . If the small nuclear contribution is ignored, the atomic magnetic moment may be taken as  $\underline{\mu} \approx \underline{\mu}_J = -g_J \mu_B \underline{J}$ . Then we see, from equation (9.35), that the transition probability for the induced emission or absorption of magnetic dipole radiation depends on the matrix elements of the perturbation operator, equation (18.22), taken between the states involved. In a weak magnetic field  $\underline{B}$  the states are correctly expressed in the coupled representation  $|\gamma JIM_F\rangle$ , while in strong external fields the uncoupled representation  $|\gamma JIM_JM_I\rangle$  is more appropriate. By applying the general considerations discussed in Chapters 5 and 7, the selection rules for magnetic dipole transitions may be obtained and are listed in the second column of Table 18.1. These transitions are labelled  $\pi$  since the polarization vector of the electric field associated with  $\underline{B}_1(t)$  is, in this case, parallel to the axis of quantization. On the other hand, when the time-dependent field has a component parallel to  $Oz$ , the transitions in Table 18.1

TABLE 18.1

*Selection rules for magnetic dipole transitions between hyperfine levels belonging to states with the same electronic angular momentum  $J$*

Static magnetic field $\underline{B}$	$\pi$ -polarization $(\underline{B}_1 \perp \underline{B})$	$\sigma$ -polarization $(\underline{B}_1 \parallel \underline{B})$
Weak	$\Delta M_F = \pm 1$	$\Delta M_F = 0$
Weak	$\Delta F = 0, \pm 1$	$\Delta F = \pm 1$
Strong	$\Delta M_J = \pm 1$	$\Delta M_J = 0$
Strong	$\Delta M_I = 0$	$\Delta M_I = 0$

labelled ' $\sigma$ -polarization' may be induced. The relative intensities of the different resonance lines may be obtained from the matrix elements given in Table 5.1 provided that the substitutions  $(j,m) \rightarrow (F,M_F)$  and  $p \rightarrow \underline{\mu}$  are made.

Additional transitions satisfying the selection rules

$$\Delta M_J = 0; \quad \Delta M_I = 0, \pm 1$$

are possible if the interaction of  $\underline{B}_1(t)$  with the nuclear magnetic moment is included. However, these will generally be too weak to be observable unless the amplitude of the r.f. field is increased by a factor of the order of  $\mu_J/\mu_I \approx 10^3$ .

*18.2. Investigation of hyperfine structure of ground-state atoms by optical pumping*

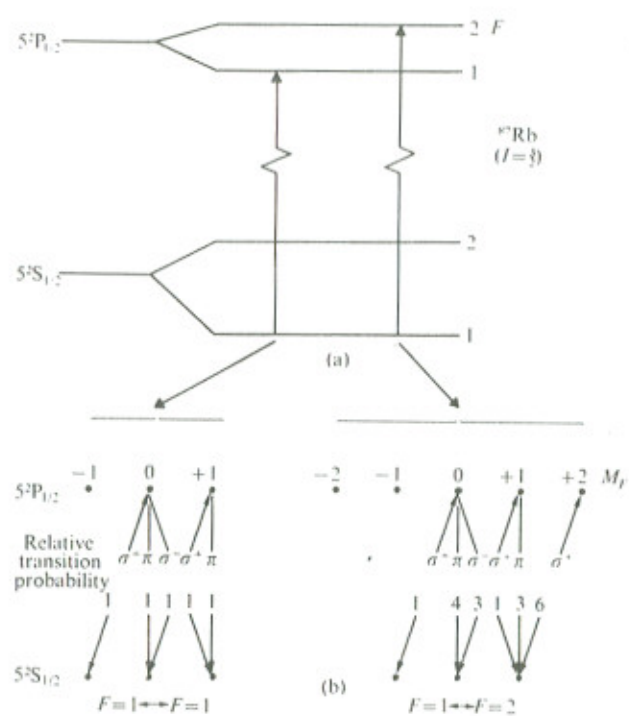


Fig. 18.4. Effect of hyperfine structure on the optical pumping cycle.  
(a) Hyperfine structure of the  ${}^2\text{S}_{1/2}$  and  ${}^2\text{P}_{1/2}$  levels of  ${}^{87}\text{Rb}$ . (b) Zeeman structure of the transitions excited by  $\sigma^+$  polarized light from the hyperfine level  $F=1$  of the ground state of  ${}^{87}\text{Rb}$ ,  ${}^2\text{S}_{1/2}$ .

18.2.1. Effect of hyperfine structure on efficiency of pumping cycle. As an example of the effect of hyperfine structure on the optical pumping process, we consider the case of  ${}^{87}\text{Rb}$  which has a nuclear spin  $I = \frac{3}{2}$ . The electronic ground state  ${}^2\text{S}_{1/2}$ , which we previously assumed to consist of a single level, is in reality split into the two hyperfine levels  $F=1$  and  $F=2$  shown in Fig. 18.4(a). The excited state  ${}^2\text{P}_{1/2}$  also consists of two hyperfine levels with the same values of  $F$  but separated by a much smaller interval than those of the ground state. In a weak magnetic field, the selection rules for electric dipole transitions between these hyperfine levels of opposite parity are the same as those for the  $(JM_J)$  quantum numbers:

$$\Delta F = 0, \pm 1 \quad ; \quad (F=0 \leftrightarrow F=0)$$

and

$$\Delta M_F = 0, \pm 1$$

(18.23)

Consequently when an optical pumping cell filled with  ${}^{87}\text{Rb}$  is illuminated with  $\sigma^+$  circularly-polarized  $D_1$  radiation from a rubidium resonance lamp, all the transitions shown in Fig. 18.4(b) will be excited for those atoms in the  $F=1$  level of the ground state. The transitions for atoms in the  $F=2$  hyperfine ground-state level are even more complex and are not shown for this reason. We see that there are many more states involved than in the case shown in Fig. 17.1, where the effect of nuclear spin was ignored, and that the transition probabilities of the different decay routes are also more nearly equal. The net result is that hyperfine structure makes the Zeeman pumping process much less efficient. This point is discussed in more detail in early papers by Hawkins (1955) and Franzen and Emslie (1957).

However, with irradiation by  $\sigma^+$  polarized light there is still a tendency for atoms to be transferred from states of low values of  $M_F$  to states of higher values of  $M_F$ , and eventually a steady state is reached in which the populations of the ground-state sub-levels are related by:

$$F=1 \quad N_1 > N_0 > N_{-1}$$

$$F=2 \quad N_2 > N_1 > N_0 > N_{-1} > N_{-2}.$$

Illumination of the cell with  $\sigma^+$  polarized light reverses the sense of the atomic polarization and pumping with linearly-polarized  $\sigma$  radiation transfers the atomic population symmetrically towards states of higher  $|M_F|$  values and results in alignment rather than orientation of the sample.

18.2.2. Zeeman magnetic resonance in  $^{85}\text{Rb}$  and  $^{87}\text{Rb}$ . These differences of population created between hyperfine Zeeman sub-levels enable magnetic resonance signals to be observed in optical pumping experiments. As an example we now consider the low frequency Zeeman transitions,  $\Delta F=0$ ,  $\Delta M_F = \pm 1$ , in an optical pumping cell containing a natural mixture of the two rubidium isotopes,  $^{85}\text{Rb}$  and  $^{87}\text{Rb}$ . The basic properties of these isotopes are listed in Table 18.2 along with those of other alkali atoms required later in this chapter.

TABLE 18.2

<i>Basic atomic parameters of alkali atoms</i>				
Atom	Natural abundance (per cent)	$I$	$\mu_I$ (nuclear magnetons)	$v_{\text{HFS}}$ (MHz)
$^6\text{Li}$	7.5	1	0.8220	228.2
$^7\text{Li}$	92.5	3/2	3.2564	803.5
$^{23}\text{Na}$	100	3/2	2.2176	1772
$^{39}\text{K}$	93.2	3/2	0.3914	461.7
$^{41}\text{K}$	6.8	3/2	0.2148	254.0
$^{85}\text{Rb}$	72.2	5/2	1.3527	3036
$^{87}\text{Rb}$	27.8	3/2	2.7506	6835
$^{133}\text{Cs}$	100	7/2	2.579	9193

(a) Resonances observed in low-resolution experiments. When the optical pumping cell is prepared without a wall coating and contains no buffer gas, the magnetic resonance signals have a line width of 10-20 kHz. The resolution is then relatively low and at fields of the order of  $1 \text{ G} = 10^{-4} \text{ T}$  only two resonance signals are observed, as shown schematically in Fig. 18.5(a). The reason for this is as follows: in low fields the Zeeman splitting is described by the hyperfine Landé g-factor, equation (18.18), which may be written approximately as

$$g_F \approx g_J \left\{ \frac{F(F+1)+J(J+1)-I(I+1)}{2F(F+1)} \right\}. \quad (18.24)$$

Since the ground-state hyperfine levels of a particular rubidium isotope are given by  $F=I \pm \frac{1}{2}$ , we find that equation (18.24) leads to identical g-values, differing in sign:

$$g_F(F=I \pm \frac{1}{2}) = \pm g_J/(2I+1). \quad (18.25)$$

Thus, in this approximation, the magnetic resonance transitions  $\Delta M_F = \pm 1$  between the hyperfine levels of a given isotope all occur at the same value of the static field  $B$  determined by

$$\hbar \omega_0 = g_F \mu_B B \approx \frac{g_J \mu_B B}{2I+1} \quad (18.26)$$

where  $\omega_0/2\pi$  is the frequency of the r.f. field. In this rubidium optical pumping experiment the observation of two well-resolved resonances is just due to the presence in the cell of two isotopes having different values of the nuclear spin  $I$ . From equation (18.26) it follows that these low-field Zeeman resonances provide a simple means of determining the nuclear spin  $I$  provided that the Landé factor  $g_J$  is known, which is usually the case. In a fixed field of 1 G the resonances in rubidium occur at the frequencies  $\omega_0/2\pi$  given by

$$\omega_0(^{85}\text{Rb}) = 467.081 \text{ kHz}$$

$$\omega_0(^{87}\text{Rb}) = 700.621 \text{ kHz}$$

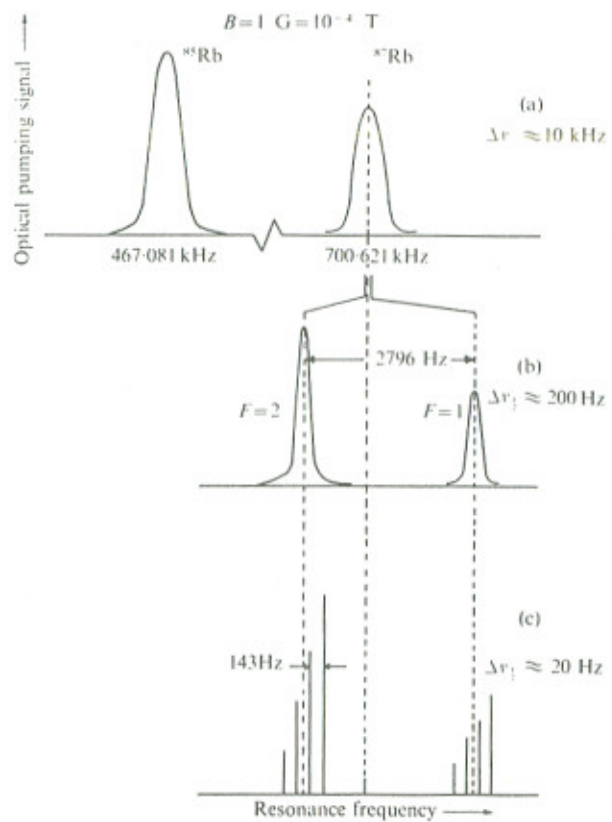


Fig. 18.5. Schematic diagram showing the effect of hyperfine structure on optical pumping magnetic resonance experiments in rubidium vapour.

(a) Signal observed with uncoated cell filled with natural isotopic mixture of  $^{85}\text{Rb}$  and  $^{87}\text{Rb}$ ; low-resolution experiment. (b) Signal observed with coated or buffered cells containing  $^{87}\text{Rb}$  only; moderate-resolution experiment. (c) Signal observed with coated or buffered cell in a uniform magnetic field; high-resolution experiment on  $^{87}\text{Rb}$ .

and it is then a straightforward exercise (Problem 18.6) to show that  $^{85}\text{Rb}$  and  $^{87}\text{Rb}$  have nuclear spins of  $I=5/2$  and  $3/2$  respectively.

(b) Resonances observed in medium-resolution experiments.

When the width of the magnetic resonance signals is reduced to  $\approx 200$  Hz by the use of suitably coated or buffered optical pumping cells, it is found that each of the broad resonances discussed in the previous section is resolved into two separate signals, as shown in Fig. 18.5(b) for the case of  $^{87}\text{Rb}$ . Now we can no longer ignore the term in equation (18.18) which involves the nuclear g-factor,  $g_I$ , and we find that the hyperfine levels  $F=I \pm \frac{1}{2}$  belonging to a given isotope have slightly different effective g-factors,  $g_F$ . In a fixed magnetic field  $B$  the resonance frequencies are given by

$$\hbar\omega_0(F=I + \frac{1}{2}) = \frac{\mu_B B}{(2I+1)} (g_J - g_I 2I \frac{m}{M}) \quad (18.27)$$

and

$$\hbar\omega_0(F=I - \frac{1}{2}) = \frac{\mu_B B}{(2I+1)} (g_J + g_I 2(I+1) \frac{m}{M}).$$

In  $^{85}\text{Rb}$  and  $^{87}\text{Rb}$  these resonances are separated by 824.9 Hz and 2796.1 Hz respectively in a field of 1 G. From these splittings of the low-field Zeeman resonances, approximate values of the nuclear magnetic moments may be determined (Problem 18.7) and the results compared with those given in Table 18.2.

(c) Resonances observed in high-resolution experiments. In optical pumping experiments with rubidium it is possible to reduce the magnetic resonance linewidth still further by careful design of the magnetic field coils and preparation of the optical pumping cell. When  $\Delta v_{1/2} < 20$  Hz it is found that all the different transitions,  $\Delta F=0$ ,  $\Delta M_F = \pm 1$ , within a single Zeeman multiplet are well resolved even in fields as low as 1 G, as shown in Fig. 18.5(c). We are now observing the very first effects of the decoupling of the nuclear

and electronic angular momenta which occurs at high fields. The Zeeman sub-levels for a given total angular momentum quantum number  $F$  are no longer equally spaced, as Fig. 18.3 clearly demonstrates, and consequently each of the composite resonances observed in the case of moderate linewidth is resolved into  $2F$  separate resonance signals. By expanding the last term in equation (18.20) for the case of small magnetic fields,  $g_J \mu_B B \ll A_J$ , it can be shown (Problem 18.8) that each resonance is separated from the next by an amount

$$\Delta v_0 = \frac{2v_{\text{HFS}} x^2}{(2I+1)^2} = \frac{2v_0^2}{v_{\text{HFS}}}. \quad (18.28)$$

In  $^{85}\text{Rb}$  and  $^{87}\text{Rb}$   $\Delta v_0$  has the values of 144 Hz and 143 Hz respectively in a field of  $10^{-4}$  T, and from this information very approximate values of the zero-field hyperfine separation  $v_{\text{HFS}}$  can be calculated.

The hyperfine separations and the hyperfine structure constants  $A_{1/2}$  can be determined much more accurately either by increasing the magnetic field  $B$  and following the  $\Delta F=0$  resonances into the intermediate field region, or more directly by studying the  $\Delta F=\pm 1$  transitions between the different hyperfine levels as we shall now describe.

### 18.3. Hyperfine pumping and the measurement of $v_{\text{HFS}}$ .

**18.3.1. Hyperfine pumping.** As we emphasized in Chapter 17, optical pumping was initially developed to produce differences of populations among the Zeeman sub-levels of the ground state. When this state also possesses hyperfine structure, a detailed analysis of the pumping process shows that there is simultaneously a tendency to concentrate atoms in the upper hyperfine level when  $\sigma^+$  polarized light is used. However, if the atoms are illuminated by a beam of radiation containing all the hyperfine components of the resonance line this hyperfine pumping is very inefficient, and the population differences created between levels with different values of  $F$  are always rather small owing to the rapidity of the

competing relaxation processes.

Much larger differences of populations between the different hyperfine levels can be created by suitably altering the relative intensities of the hyperfine components of the pumping lamp. Since these components are very close together conventional interference filters cannot be used, but fortunately in many cases the natural displacement between the resonance lines of different isotopes of an element enables selective light sources to be constructed. This is especially true in mercury, as shown by Table 16.1, and in the case of rubidium which we consider now.

The energy levels and hyperfine structure of  $D_1$  resonance line of rubidium at  $7947 \text{ \AA}$  are shown in Fig. 18.6 for the naturally occurring isotopes  $^{85}\text{Rb}$  and  $^{87}\text{Rb}$ . The hyperfine intervals in the excited state  $5^2P_{1/2}$  are small compared with the Doppler width and the resonance line of each isotope consists of only two components labelled A, B for  $^{85}\text{Rb}$  and a, b for  $^{87}\text{Rb}$ . The relative positions of these components are shown in Fig. 18.6(b). Components A and a are nearly coincident and overlap because of Doppler broadening, while components B and b are well resolved. Hyperfine pumping is now possible with a number of different combinations of isotopically separated lamps, filters, and pumping cells.

For instance, if a cell containing  $^{87}\text{Rb}$  is illuminated with light from a  $^{85}\text{Rb}$  lamp only the component A will be absorbed, pumping atoms from the upper hyperfine level  $F=2$  of the ground state. The population of the hyperfine level  $F=2$  of the  $^{87}\text{Rb}$  atoms in the cell will decrease while the population of the lower level  $F=1$  increases.

Alternatively if light from a  $^{87}\text{Rb}$  lamp is passed through an absorption cell containing  $^{85}\text{Rb}$ , only the b component of the lamp will be transmitted by the filter. When this light is focussed into an optical pumping cell containing  $^{87}\text{Rb}$  atoms the b component preferentially pumps the atoms from the  $F=1$  to the  $F=2$  ground-state hyperfine level.

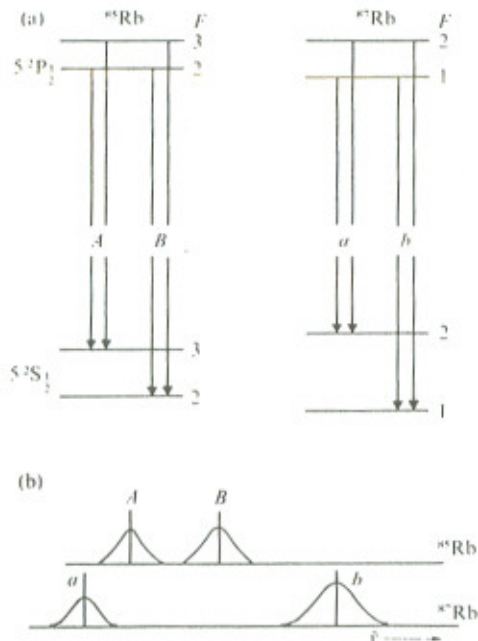


Fig. 18.6. Hyperfine structure of the  $D_1$  resonance line ( $5^2S_{1/2} - 5^2P_{1/2}$ ) of  $^{85}\text{Rb}$  and  $^{87}\text{Rb}$ ; (a) energy levels; (b) hyperfine structure components of the  $D_1$  line.

In either case the resulting population difference enables the hyperfine magnetic resonance transitions  $\Delta F = \pm 1$  to be detected when microwave power at 6835 MHz is fed into the optical pumping cell. Analogous techniques can be used to achieve hyperfine pumping in the mercury isotopes  $^{199}\text{Hg}$  and  $^{201}\text{Hg}$  as inspection of Table 16.1 reveals.

**18.3.2. Measurement of the hyperfine interval  $\nu_{\text{HFS}}$ .** The magnetic resonance transition  $\Delta F = \pm 1$ ,  $M_F = 0 \leftrightarrow M_F = 0$  is usually chosen for the measurement of the hyperfine interval

$\hbar\nu_{\text{HFS}}$  since this particular transition depends on the magnetic field only through a second-order term which is very small in weak fields. According to the Breit-Rabi formula, equation (18.20), the frequency of this transition is given by (Problem 18.9)

$$\nu_0 = \nu_{\text{HFS}}(1 + x^2/2). \quad (18.29)$$

The frequencies of the nearest other hyperfine transitions  $\Delta F = 1$ ,  $M_F = 0 \leftrightarrow M_F = \pm 1$  are strongly field dependent:

$$\nu_0 = \nu_{\text{HFS}} + \frac{g_J \mu_B B}{\hbar(2J+1)} \quad (18.30)$$

and may be separated from the main  $(0,0)$  resonance by applying an external magnetic field of the order of  $10^{-2} - 10^{-1}$  G. In fact the frequency of these field-dependent transitions can be used to make an exact evaluation of the quadratic term in equation (18.29), thus leading to a precise measurement of  $\nu_{\text{HFS}}$ . In these experiments the uncertainty in the measured field values leads to a relative error in the determination of the hyperfine interval of  $\Delta\nu_0/\nu_{\text{HFS}} \approx 10^{-11}$ , provided that the effects of the light and pressure shifts discussed below are eliminated.

